DEMODULATION OF FIBER OPTIC SENSORS FOR ULTRASOUND DETECTION AND STRAIN MEASUREMENT

By

Abu Farzan Mitul

A DISSERTATION

Submitted to
Michigan State University
in partial fulfillment of the requirements
for the degree of

Electrical Engineering – Doctor of Philosophy

2023

ABSTRACT

Optical fiber sensors are employed to study and investigate several physical-related parameters e,g, pressure, stress, vibration, rotation, current, bending, displacement etc. Fiber optic sensor (FOS) technology is associated with optical related accessories e,g, light processing (filters), optical source (laser, LED), optical detector (spectrometer. photodiode), light guiding (lenses) etc. In addition to the use of FOS technology, laser Diode (LD) has great deal of importance due to its easy integration, small size and moderate price. Semiconductor lasers are complex nonlinear systems where relatively small optical feedback can have a profound impact on the spectral and temporal behavior of the laser output. Under appropriate conditions, optical feedback provides a straightforward and highly effective way for laser linewidth reduction. These conditions can be met in the so-called self-injection locking [1, 2] or filtered optical feedback [3, 5] configurations where part of output light, after passing through an optical resonator, is injected back to the laser to interfere coherently with the light inside the laser internal cavity. Due to the excellent noise performance and straightforward implementation, fiber-pigtailed lasers under self-injection locking have been studied as light sources for fiber-optic sensor systems whose performance is sensitive to laser frequency noises such as phase-sensitive optical time-domain reflectometry systems and fiber-optic gyroscopes [6, 7, 8].

We present a method to suppress the wavelength drift of a semiconductor laser with filtered optical feedback from a long fiber-optic loop. The laser wavelength is stabilized to the filter peak through actively controlling the phase delay of the feedback light. A detailed steady-state analysis of the laser wavelength is performed to illustrate the method. Experimentally, the wavelength drift was reduced by 75% compared to the case without phase delay control.

The long optical feedback length makes the lasers prone to mode-hopping. There have been reported attempts at suppressing mode-hopping by light polarization control and using more compact resonator [6, 7] but no detailed characterization of mode-hopping and the associated laser instability has been reported. We studied the mode-hopping and laser instability of the self-injection locked laser and found that a mode hopping event causes an abrupt change in the laser intensity after the resonator inside the feedback loop. Experiment shows that the frequency of locked lasers could oscillate during unstable operations.

We demonstrate the use of a self-injection locked distributed feedback (DFB) diode laser for high-sensitivity detection of acoustic emission (AE) using a fiber-coil Fabry-Perot interferometer (FPI) sensor. The FPI AE sensor is formed by two weak fiber Bragg gratings on the ends of a long span of coiled fiber, resulting in dense sinusoidal fringes in its reflection spectrum that allows the use of a modified phase-generated carrier demodulation method. The demodulation method does not require agile tuning capability of the laser, which makes the self-injection locked laser particularly attractive for the application. Little work has been reported on using self-injection locked lasers in fiber-optic AE or ultrasonic sensor systems due to the challenges induced by the lack of the agile wavelength tuning capability of a self-injection locked laser. Experimental results indicate that the self-injection locked laser increases the signal-to-noise ratio by ~33 dB compared with the free-running DFB laser.

Furthermore, we have developed a low-cost fiber-optic sensor system that can measure absolute strain at multiple positions along a fiber using fiber-bragg grating sensors. In this system, we form a “rf interferometer” with low order fringes to ensure that the strain-induced rf spectral shift does not exceed half of the fringe period, rendering the possibility of absolute strain measurement.

ACKNOWLEDGEMENTS

I would like thank my supervisor Dr. Ming Han for his continuous support, guidance and encouragement in completing these research projects. I appreciate the time and efforts of all committee members, Dr. Wen Li, Dr. Nelson Sepulveda Alancastro and Dr. Zhen Qiu.

TABLE OF CONTENTS

Chapter 1: Introduction

1.1. Research Objective and Motivation of the work

Optical fibers are being used in the field of sensor and communication applications for several years. Optical fiber sensors have several advantages over electrical and mechanical sensors. The fiber is fabricated either from plastic or glass (silica) and it is electrically passive. For this reason, there are immunity to external electromagnetic interference in fiber optic sensors. Fiber optic sensors (FOSs) [9] can be mechanically robust and light weight due to its small size of fiber. In case of harsh environments i,e, high radiation [10], high temperature, strong shock or, vibration; the fiber optic sensors can sustain and perform well [11]. FOSs have gone through extraordinary development, advancement and growth in past few years. The telecommunication industry has been revolutionized through reliable and higher performance telecommunication links of fiber optic communication industry. In addition to this development, fiber optic gyroscopes, chemical probes, sensors of vibration, pressure [12], temperature [13] are in the spotlight of FOS advancement [14]. Fiber waveguide is the key sources to provide high average power, excellent beam quality and wall-plug efficiency here [14, 15, 16].

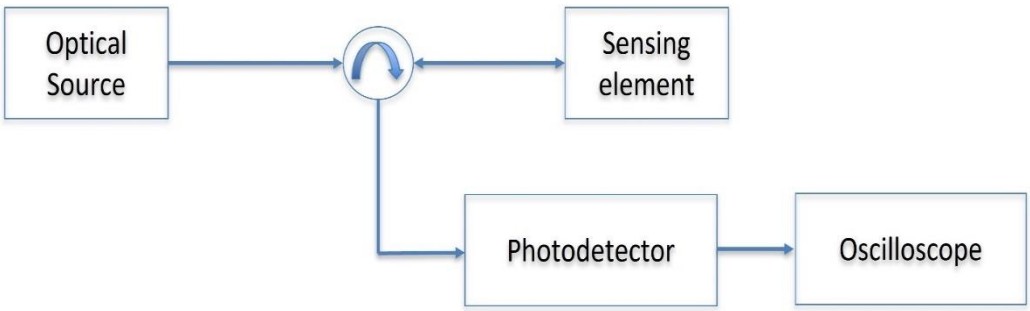

Figure 3.1 General structure of fiber optic sensing technology.

Figure 1-1 shows a general structure of FOS system. In the sensing system, optical source can be in form of laser diode, laser, LED etc. The sensing element can be fiber bragg gratings,

fiber coil sensors etc. Light from optical source passes through circulator and reflects back from sensing element. The changes in optical signal is detected through photodetector and actuating circuitry (e,g, oscilloscope, processing electronics, optical spectrum analyzer etc.). The optical signal can be modulated before it arrives to the sensing element so that the sensor spectrum can appear through photodetector/ oscilloscope.

Many damage-related structural changes, such as crack initiation, crack growth, and fiber breakage, are accompanied by a sudden release of stress energy, leading to the generation of transient elastic waves typically in the frequency range of 20 kHz to 1 MHz. These waves are called acoustic emission (AE) and its detection has been widely used for structural health monitoring. Traditionally, piezoelectric sensors are used for AE detection. Piezoelectric transducer (PZT) sensor is one of the most popular AE detection device due to it`s good stability and sensitivity. PZT AE sensor can be operated over a limited range of temperature and susceptible to stress corrosion and electromagnetic interference. Moreover, it requires lead-in and lead-out wires and due to the durable nature, it is not suitable to embed in materials. Recently, fiber-optic AE sensors, especially those based on fiber Bragg gratings (FBGs), have become an attractive alternative and are being intensively studied because they provide several advantages such as light weight, small size, corrosion resistance, multiplexing capabilities, and immunity to electromagnetic interference [18]. Because of the required detection speed, these sensors are typically demodulated by the edge filter detection technique, in which the wavelength of a tunable laser is locked on the slope of the spectral features of the sensor to convert AE-induced spectral shift to the intensity variations of the reflected laser light [18, 19, 20]. Detection sensitivity (characterized by the minimum detectable wavelength shift) is a key performance parameter of fiber-optic AE sensors. Previous effort to improve the detection sensitivity has been focused on

increasing the slope of the spectral feature through FBG-based optical resonators such as chirped FBG Fabry–Perot interferometers (FPIs) [22] or π-phase-shifted FBGs [22, 23], which can generate narrow resonant features with spectral width on the order of 1 pm in the 1550 nm wavelength window. Figure 1-2 shows fiber coil sensor where fiber length between FBGs: (e.g. ~40 cm) and Figure 1-3 shows sinusoidal fringes of fiber coil sensor with a free-spectral range of ~ 2 pm. Here, fringe profile is determined by the FBG reflection spectrum. Fiber coil sensor offers longer cavity length which results in a steeper slope in the spectrum and it can provide higher sensitivity. Again, fiber coil sensor has circular symmetry which helps to receive omnidirectional response.

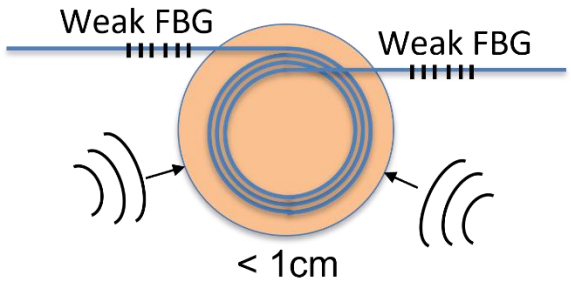

Figure 3.2 Fiber coil sensor where fiber length between FBGs: (e.g. ~40 cm).

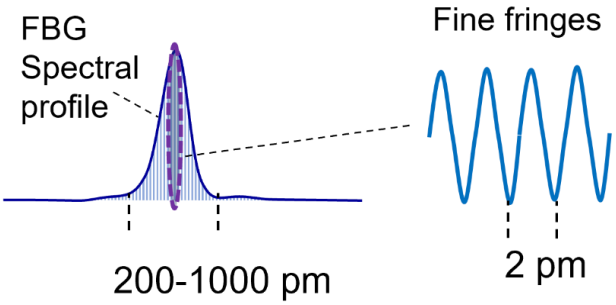

Figure 3.3 Fiber coil sensor having sinusoidal fringes with a free-spectral range of ~ 2 pm.

As the spectral slope increases, the noise of the system is ultimately dominated by the laser frequency noise, which is converted to laser intensity variations by the spectral slope and shows

up as the noise at the output of the photodetector. Locking of the laser wavelength on a narrow spectral feature also requires agile wavelength tuning capability of the laser. Therefore, a tunable laser with minimum frequency noise is critical for these advanced sensors to reach their potential of high-sensitivity AE detection.

Fiber lasers are attractive element for several applications i,e, defense, medicine, security, material processing etc [24, 25] and Ultra-narrow linewidth lasers have several applications including optical fiber sensing, coherent ranging and atomic clocks etc. Distributed feedback laser diodes (DFB-LDs) are seen to have narrow linewidth, which is typically in the range of megahertz or, less. But the free running laser frequency of DFB-LD is unstable and it`s linewidth can be narrowed, and the output spectrum can be stabilized by means of external cavity.

External cavity diode lasers (ECDLs) offer long cavity length and superior performance in terms of frequency noise compared to distributed feedback (DFB) diode lasers. Optical resonator can be utilized to lock the laser and thus stabilize the laser frequency of diode laser. Existing low frequency noise lasers for fiber-optic AE sensors are mostly external cavity diode lasers. They have a long cavity length and thus provide a high-quality factor of the laser cavity, rendering excellent frequency noise performance. However, the bulk size, the complexity of the laser cavity, the stringent optical alignment requirements, and the high cost limit their use in practical applications. As a tool for frequency noise suppression, self-injection locking technique can be utilized where laser is connected to a fiber ring and part of the laser light passes through an external resonator and finally gets injected back to the laser diode.

In self injection locking mode, laser frequency fluctuations get converted into amplitude fluctuations through external resonator and amplitude-phase coupling in laser diode converts it

back to frequency fluctuations. The frequency fluctuations with proper feedback phase adjustment destructively interfere with the original frequency fluctuations and hence, reduce frequency noise.

Here, self-injection locking is an all optical operation and compared to electronic locking schemes; it offers reduced system complexity. It is possible to lock the low cost semiconductor lasers e,g, fabry-perot diode lasers, DFB diode lasers etc. in whispering gallery mode resonator (WGMR), external ring fiber cavity, fabry-perot cavity through fiber bragg grating array.

G. Hadley et al, proposed a method in 1986 to achieve narrow linewidth high power laser where narrow frequency spectrum of low power master laser was transferred to broad-spectrum high-power slave diode laser using optical injection [27]. But, such systems are extremely sensitive to ambient conditions and very complicated. Pound-Denver-Hall (PDH) technique was found to be useful [27], [33]–[35] for active locking [27, 28, 29]. But it requires electronic feedback complex circuitry and optical modulation. Motonobu Kourogi et al, introduced side of fringe stabilization to provide locking mechanism in 1991 [31]. This technique does not need optical modulation. But it requires a stable laser intensity and the reference level.

Figure 1-2 shows the laser configuration. A small portion (weak feedback) of the linearly polarized light from a DFB diode laser is coupled back to the laser cavity through a fiber-optic loop consisting of a circulator, a coupler for coupling the light out of the loop, an in-line high-finesse Fabry-Perot (FP) interferometer as an optical filter, another coupler, and an attenuator for adjusting the feedback level. Note that the coupler after the FP is for stabilizing the laser wavelength using the proposed scheme. We further assume that the feedback light maintains its linear polarization state as it goes through the feedback loop. We only perform the steady-state analysis, which is sufficient for understanding the origins of the laser wavelength drift and the proposed method to suppress the drift.

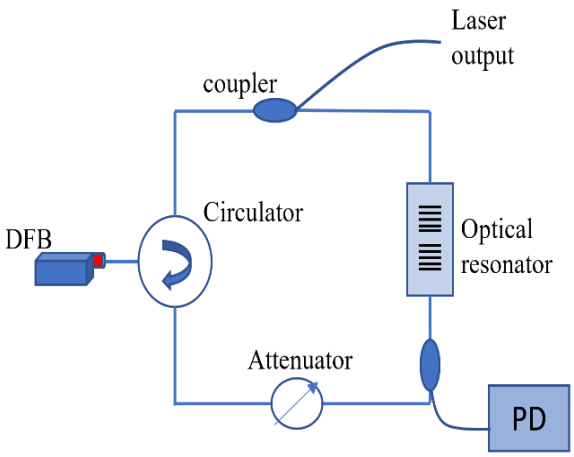

Figure 3.4 Schematic of a DFB laser with coherent filtered optical feedback.

As a result of high Q factor, resonators offer circumferential resonant path which leads to an effective pathway to narrow the linewidth of DFB-LDs. external cavities with Fabry-Perot cavity [4, 20] optical gratings also offer narrow linewidth of DFB-LD. Microdisk [5, 21], microsphere [22, 23] cavities have some drawbacks including impossible route of integration and high coupling loss. DFB-LD with fiber ring resonator as external cavity over several advantages including linewidth narrowing, low loss and low cost [24, 25, 26]. Free spectral range (FSR) is small for long optical fiber ring and for this reason, there can be frequent mode hopping during self-injection locking setup. Moreover, the long fiber ring resonator can be susceptible to external environment i,e, vibration and temperature. Frequent mode creates obstacle for the application of locked DFB-LD. Optical waveguide ring resonator has tremendous benefits include easy integration, compactness and robustness to environmental interference. It can meet up various demands as it`s size can be varied from few microns in micro ring resonators through several centimeters [38].

Fiber lasers inherit various kinds of mode instabilities. More importantly, the fiber amplifier output power is limited by transversal mode instability. Longitudinal mode instability could also trigger the self-Q-switched regime and it can turn into spectra evolution characteristics.

Self-induced laser line sweeping (SLLS) is a phenomena where output wavelength of laser can drift spontaneously. In SLLS, the laser output wavelength can drift steadily, periodically within a spectral range. Laser resonator can support many laser modes. Once laser reaches its threshold level, longitudinal mode associated with highest gain gets established and due to the resonator feedback, establishment of standing wave in cavity exists. Population inversion in excited states deplete and finally, the gain of the mode exhaust itself. As a result, this is not the mode with highest gain anymore. Meanwhile, another longitudinal mode whose power overlaps with the cavity gain areas compared to previously lasing one proceed to rise. This is a repeating process and very few or, only one can lease instantaneously. Length of cavity, speed of propagation inside cavity, mode number define the frequency of every longitudinal mode. Thus, in SLLS, central frequency of laser line moves. Again, as long as mode moves to higher gain, mode hopping happens in one direction. The process of sweeping laser line towards longer wavelength is explained through the dependence of gain peak wavelength on population inversion in [39]. With the increase in population inversion, gain curve peak of ytterbium laser moves towards shorter wavelength. Similarly, with the decrease in inversion, gain curve peak tends to longer wavelengths. Laser line sweeping direction can also be indicated through fiber bragg gratings, refractive index modulation, generated in SLLS laser cavity as reported in [15]. Like other instability of fiber lasers, SLLS effect is also considered to be instability. Moreover, sweep rate is related to active fiber length and output laser power according to [40].

It has been reported that sub-100 Hz linewidth can be achieved by self-injection locking a distributed feedback (DFB) laser to a microresonator with an ultrahigh quality factor [40], in which the output light is coupled to the resonator in free space. Figure 1-3 shows the use of WGMR for self-injection locking.

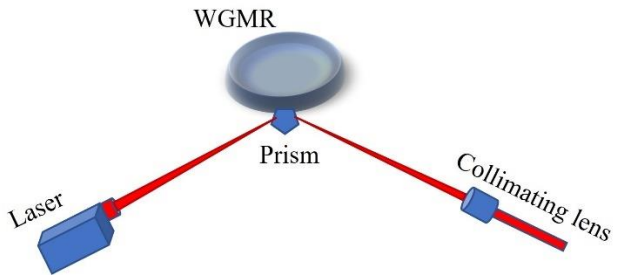

Figure 3.5 Self-injection locking of a DFB laser to a microresonator.

The free-space coupling can minimize the optical length of the feedback loop and lead to stable phase delay of the feedback light, which is important for achieving stable linewidth reduction and laser operation. However, it imposes stringent requirement on optical alignment. Optical feedback has also been applied to DFB lasers though fiber feedback loops formed by optical circulators and laser linewidth ranging from ~100 Hz to a few kHz has been achieved [27, 33, 34, 35]. The use of optical fibers alleviated the challenges in optical alignment. However, the long fiber-optic feedback loop makes phase delay of the feedback light, and, consequently, the laser operation, sensitive to environmental perturbations. The laser wavelength can drift away from the center of the resonator and eventually cause mode hopping where the locked laser wavelength jumps between the external cavity modes.

This dissertation focuses on the development of phase delay control mechanism in self injection laser. Self injection laser offers narrow linewidth, low frequency noise and innovative phase control technique can offer wavelength drift suppression.

In the field of energy and transportation sectors, civil structures e,g, dams, buildings, bridges, tunnels and pipelines play a vital role in everyday life of human being. In this regards, it has become necessary to look after the safety, cost-effectiveness, durability of these structures during the harsh environments e,g, floods, fire, earthquakes etc. Many people may affect financially due to the closure or, significant damages of the bridges or, such structures. Due to such importance in daily life, it has become compulsory to monitor the condition of structure and provide adequate maintenance. Visual inspection was used to track the conditions of civil structures due to its ease of use and low cost. But, visual inspection is subjected to human error because of its sole dependence on inspector`s experience and understanding. Moreover, visual inspection can not accurately describe the condition of the system (i,e, load bearing capacity, lifespan). Due to the social dependence on these structures in everyday life, it has become part and parcel to maintain structural health monitoring (SHM) in efficient way.

In order to lead a structure e,g, civil, aerospace, ship and mechanical engineering etc to a safer direction at cheap rate, its necessary to possess SHM. During manufacturing or, in-service operation, SHM systems can assess structural integrity which allow the improvement in quality, timely maintenance, optimal operation and longer service life. During in-service operation, SHM system identifies the load applied to a structure or, cracks in it. Knowing the structural capacity (like, stiffness, strength); it is possible to identify whether the load is within the tolerance limit of structure. It is necessary to monitor the load and damage simultaneously so that existing defect or, excessive loading can be avoided. Lack of inherent stiffness or, strength in structure can cause harmful deformation or, critical failure. Non-destructive inspection (NDI) can find the damages right away. If the structure is embedded with sensors, it is possible to detect the damages. Damage sensors can only provide information regarding the damages and associated cracks in it. SHM

assists in avoiding damage and provides lower maintenance cost [36, 37]. Throughout the process of early detection of structures, significant deterioration can be avoided. Furthermore, the repairing cost can be minimized and lifespan of structures can increase [46].

Modern aircraft structures consist of materials with low structural elements and high mechanical strength. To meet this criteria, modern materials are being used in aviation industry e,g, composite materials. These materials possess complex construction. Each composite part of the material have specific amount of layers and they work differently which depends on the forces acting and fibers in it. Many structural damages and failures can occur in the construction of modern aircrafts. These structural failure takes place due to the defects in material microstructure, holes, manufacturing errors, radii, cutouts, tight rounding etc [47]. NASA``s Helios wing faced in-flight break-up in 2003. Excessive wind deformation might be the most probable reason behind such failure. There was a need for development of robust shape-detection methodology by NASA Dryden Flight Research Center (DFRC) [48].

Strain can provide information regarding the structural deformation, and it is also considered as a sensitivity to damage on structures due to excessive load [49]. Detection of damage is not same as the measurement of strains. Damage is referred to as the local change in material properties or, at the boundaries of structure which eventually reduces the structural performance. Crack diminishes the strength of the structure by larger rate. Prior to catastrophic failure, it generates minor changes in structural parameters (e,g, global strain fields, natural frequencies etc). SHM system requires to be maintained periodically for its proper functionality.

Several SHM systems include accelerometers [42, 43, 44, 45], inclinometer [46, 47, 48, 49, 50], total station surveys [51, 52, 53], extensometers [54, 55, 56, 57], wave propagation [58, 59,

60, 61, 62] and acoustic emission [38, 63, 64, 65, 66]. Optical fiber was used for damage detection in 1990 with the heading named, “structures with nerves of glass” [40, 41].

Fiber optic strain sensors (FOSS) has several advantages including light weight, high signal-to-noise ratio, immunity to electromagnetic interference and small size. Due to the property of flexibility and deformability of optical fibers along with great optical performance, FOSS can sustain in large strain load [77].

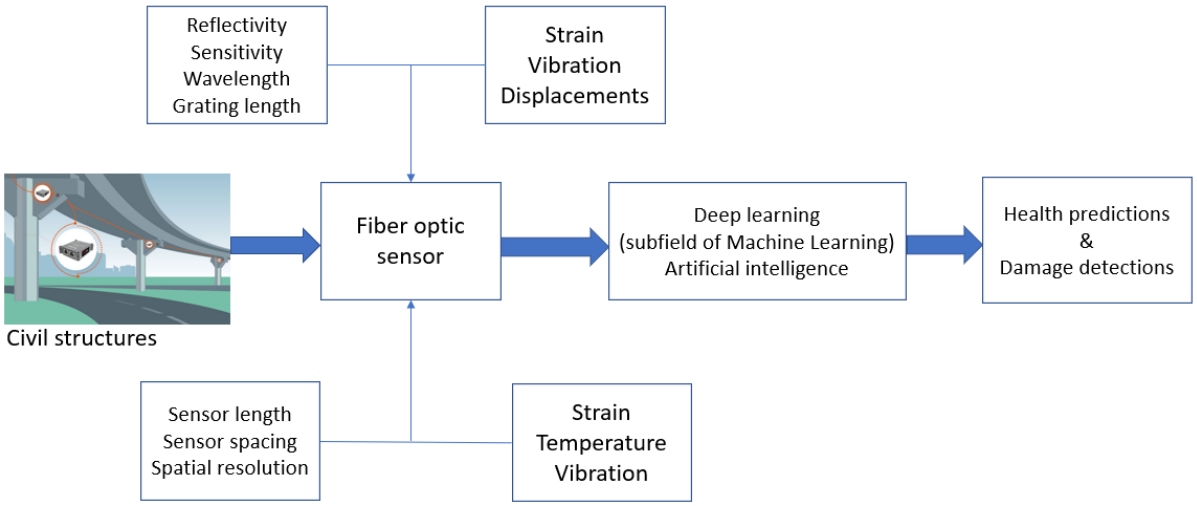

Figure 3.6 Fiber optic sensor in Structural health monitoring of civil structures based on deep learning [46].

Figure 1-4 shows the use of FOSS and deep learning in SHM for health predictions and damage detections. As a result SHM system depends on the volume of data capture, FOSS accuracy and effectiveness of data processing algorithms. Sensors collect a wide varieties of data include ultrasonic, displacement, acceleration, strain, global positioning system etc. For the application of SHM, Kalman filter approaches, Bayesian approaches, machine learning approaches, fuzzy logic approaches, DS approaches etc can be used as data fusion techniques [78].

In this dissertation, we also have demonstrated the demodulation of fiber optic sensors for strain measurement.

1.2. Dissertation organization

This dissertation is composed of four chapters where Chapter 2 focuses on the development of rate equation model which can describe the functionality of a DFB laser with coherent filtered optical feedback and a longer fiber ring was used in the process. In this section, time evolution of electric field complex amplitude inside the laser cavity and the effect of external loop with multiple optical paths are also discussed. Considering cavity loss and waveguide loss inside the laser cavity, rate equation for the cavity with filtered optical feedback (fiber ring) is developed. A relation between the free running laser frequency to locked laser frequency is also discussed in this section. Furthermore, stable solutions to lock the laser wavelength for a given free running operating wavelength are identified. Multiple optical locking points are simulated around the fabry perot (FP) transmission peak. Steady state solutions of three phase delays are also developed which correspond to three different optical path length of feedback loop.

Chapter 3 illustrates the experimental setup to demonstrate different phase delays of feedback light in self injection locking circuit. A cantilever beam with fiber structure was developed to identify the phase delays in feedback loop. The amplitude and phase relationship from the feedback path is investigated for different phase delays. More specifically, three operating points are observed on FBG-FP transmission spectrum. Positive slope, negative slope and peak of FBG-FP transmission spectrum provided in-phase. Out of phase and double frequency component relative to modulation signal in FBG-FP spectrum. Furthermore, a feedback control system is developed using the feedback light of self-injection locking setup. The controller output is fed to the motorized stretcher which precisely moved based on the input provided by feedback light and

thus control the phase delay. The feedback control was run to pin the laser wavelength around the center of FBG-FPI transmission spectrum. Moreover, linewidth of free running laser and self-injection locked laser are measured using delayed self-heterodyne technique in this section. Differences in beat note spectra is observed between with and without phase delay control setup.

Chapter 4 focuses on the mode hopping signal of self-injection locked laser where, a broadband dc-coupled un-amplified photodetector with a bandwidth from dc to 1.2 GHz is used to observe the overall signal and an amplified photodetector with both an ac (25 kHz-125 MHz) output and a quasi-dc (dc-50 kHz) output are also utilized in the experimental setup. In this section, stable and unstable laser operation are also monitored. Periodic oscillation of laser instable operation has an effect with the delay time of feedback light. Self-injection locked laser frequency oscillation is analyzed compared to the laser output.

Chapter 5 demonstrates the application of a self-injection locked distributed feedback (DFB) diode laser for high-sensitivity detection of acoustic emission (AE) utilizing a fiber-coil FPI sensor. This chapter focuses on the mode-hopping and laser instability of the self-injection locked laser and their effect on the demodulated signal and it is found that a mode hopping event causes an abrupt change in the laser intensity after the resonator inside the feedback loop. It manifests itself as a short transient signal in the output of the AE sensor system. It is also observed that, frequency of mode-hopping occurrence is related to the length of the feedback loop and reducing the loop length can effectively reduce the frequency of mode-hopping occurrence.

Chapter 6 investigates a novel approach for the measurement of absolute strain using fiber-optic sensors and Chapter 7 discusses the research outcome from this dissertation and future research aspects in the field of FOS system.

Chapter 2: Simulation of Semiconductor Laser with Filtered Optical Feedback

Part of the material in this chapter has been published in "A. Mitul and M. Han*, "Wavelength drift suppression of semiconductor laser with filtered optical feedback from fiber-optic loop using active phase-delay control," Optics Letters, 47, 5457-5460 (2022).

In this chapter, we have analyzed the self-injection locked DFB laser and developed a model which describes the dependency of phase delay of feedback light on fiber ring length. Electric field complex amplitude in the cavity, equivalent amplitude reflectivity, cavity loss for the laser cavity, waveguide loss of the laser cavity equations are considered throughout the process.

2.1. Rate equation for the laser cavity with the filtered optical feedback

In order to find out the rate equation of laser cavity with filtered optical feedback, we considered the time evolution of the electric field complex amplitude in the cavity, $E(t)$ as described in [2] where laser cavity without optical feedback is considered. The equation for time evolution of the electric field complex amplitude in the cavity is as follows:

$$\frac{d}{dt}\left(E(t)e^{i\omega t}\right)=\left[i\omega_N+\frac{1}{2}(G-\Gamma_0)(1+i\alpha)\right]E(t)e^{i\omega t}, \tag{2.1}$$

where ω is the frequency of the electric field, $\omega_N = N\pi c/\eta l_d$ is the laser cavity mode frequency (operating frequency of laser without optical feedback), N is the order of the laser cavity mode, c is the speed of light in vacuum, η and l_d are, respectively, the refractive index and length of the laser optical cavity, G is the net rate of stimulated emission, Γ_0 is the laser cavity loss including the waveguide loss and the mirror loss in the diode cavity, and α is the phase-amplitude coupling factor.

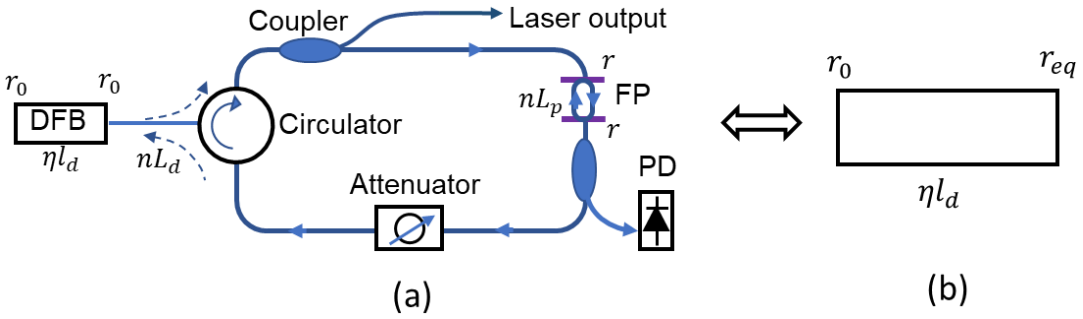

Figure 3.2 Laser diode with filtered optical feedback (a) can be modeled by a laser cavity with an equivalent amplitude reflection coefficient (b).

In the filtered optical feedback configuration shown in Figure 2-1(a), a portion of laser output is coupled back to the laser cavity through a fiber-optic loop with a high-finesse Fabry-Perot (FP) interferometer. The effect of the external loop with multiple optical paths can be described, as shown in Figure 2-1(b), by a simple laser cavity with an equivalent amplitude reflectivity [79] for the laser facet on the right given by

$$r_{eq}=r_0+\sqrt{\beta}\left(1-r_0^2\right)\left(1-r^2\right)e^{-i\omega\tau_d}\sum_{m=0}^{\infty}r^{2m}e^{-i2m\omega\tau_p}, \tag{2.2}$$

where β represents the feedback power factor including the loss from the fiber coupler and the attenuator in the feedback loop and the coupling loss at the front facet of the laser cavity due to the mode mismatch, and r and r_0 are, respectively, the amplitude reflection coefficients of the FP mirrors (assumed identical) and the facets (also assumed identical) of the laser optical cavity. Note that the multiple beam reflections from the laser facet are ignored in Eq. (2.2). The cavity loss for the laser cavity, Γ, can be computed by [80]

$$\Gamma=\Gamma_w-\frac{c}{\eta l_d}\ln\left(r_0 r_{eq}\right), \tag{2.3}$$

where Γ_w is the waveguide loss of the laser cavity. Plugging Eq. (2.2) into Eq. (2.3) and assuming weak feedback, we have

$$\Gamma \approx \Gamma_0 - \frac{c}{\eta l_d}\sqrt{\beta}\left(\frac{1-r_0^2}{r_0}\right)(1-r^2)\sum_{m=0}^{\infty} r^{2m} e^{-i\omega(2m\tau_p+\tau_d)}. \quad (2.4)$$

Note that Γ_0 is cavity loss without the optical feedback. The second term on the right-hand side of Eq. (2.4) indicates that cavity loss due to the feedback loop can be considered as a linear combination of a series of losses, each of which is associated with a beam path of the feedback light. The damping rate of the electric field in the cavity is equal to $\frac{1}{2}\Gamma Ee^{i\omega t}$ [80]. Adding the feedback terms in Eq. (2.4) to Eq. (2.1), we obtain the rate equation for the laser cavity with the filtered optical feedback

$$\frac{d}{dt}\left(E(t)e^{i\omega t}\right) = \left[i\omega_N + \frac{1}{2}(G-\Gamma_0)(1+i\alpha)\right]E(t)e^{i\omega t} + \sum_{m=0}^{\infty} K_m E(t-\tau_m)e^{i\omega(t-\tau_m)}, \quad (2.5)$$

where $\tau_m = \tau_d + 2m\tau_p$ is the time delay caused by the fiber loop for the beam that goes through m round trips in the FP. The K_m coefficients are given by

$$K_m = \frac{c}{2\eta l_d}\sqrt{\beta}\left(\frac{1-r_0^2}{r_0}\right)(1-r^2)r^{2m}. \quad (2.6)$$

In the case of steady state, we can obtain an equation relating the free-running laser frequency, ω_N, to the locked laser frequency, ω, following similar processes in [2] involving setting E(t) to be independent of time and separating the real and imaginary parts in Eq. (2.5), which leads to Eq. (2.7). The steady-state analysis leads to an equation relating the free-running (without optical feedback) laser frequency, ω_N, to the locked laser frequency, ω, given by

$$\omega_N = \omega + K\frac{\sin(\omega\tau_d+\theta) - r^2\sin(\omega(\tau_d-2\tau_p)+\theta)}{1+F^2\sin^2\omega\tau_d} \quad (2.7)$$

where $F = 2r/(1-r^2)$, r is the amplitude reflection coefficients of the FP mirrors (assumed identical), $\theta = \tan^{-1}\alpha$, α is the phase-amplitude coupling factor, τ_d is the time delay

from a single trip of the fiber loop including a single pass of the FP, τ_p is the time delay from a one-way trip of the FP cavity length ($\tau_d = nL_d/c$ and $\tau_p = nL_p/c$, where nL_d and nL_p are, respectively, the optical length of the feedback loop and the FP cavity). The coefficient K is given by

$$K=(1+\alpha)^{\frac{1}{2}}\frac{c}{2\eta l_d}\sqrt{\beta}\left(\frac{1-r_0^2}{r_0}\right)\left(\frac{1}{1-r^2}\right) \quad (2.8)$$

where β represents the feedback power factor including the loss from feedback loop and the coupling loss at the front facet of the laser cavity, r_0 is the amplitude reflection coefficients of the laser cavity facets (assumed identical), ηl_d is the optical length of the laser cavity, and c is the speed of light in vacuum.

2.2. Demonstration of change in phase delay of feedback light by changing the fiber ring length

We consider a case of a long feedback loop with an optical length of $nL_d = 14.5$ m and an FP cavity with a power reflectivity $r^2 = 96\%$ for the mirrors and a cavity optical length of $nL_p = 1.45$ cm, resulting in FP transmission peaks with a 3-dB width of 1.1 pm at 1550 nm, as shown in Figure 2-2.

The rest of the system parameters are $\eta l_d = 1.02$ mm, $r_0^2 = 36.6\%$, $\alpha = 5$, and $\beta = -15$dB. Figure 2-3 shows the relationship between the free-running laser wavelength $\lambda_N = 2\pi c/\omega_N$ and the optically locked wavelength $\lambda = 2\pi c/\omega$, both relative to the wavelength of the FP transmission peak, λ_0 ($\Delta\lambda_N = \lambda_N - \lambda_0$ vs. $\Delta\lambda = \lambda - \lambda_0$).

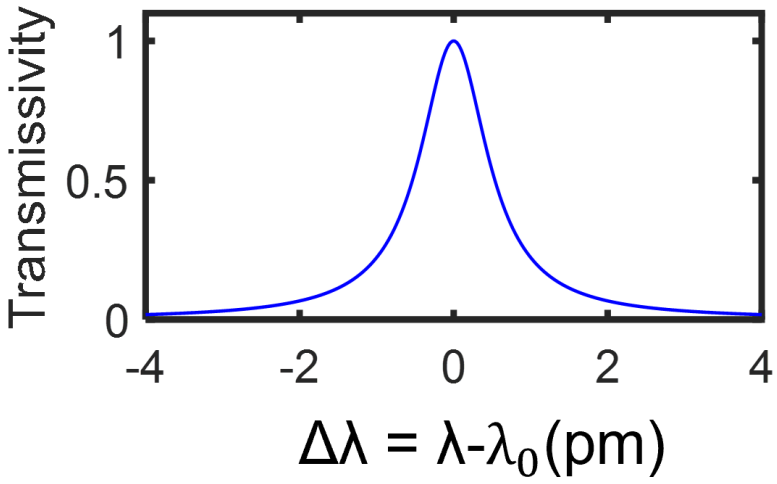

Figure 3.3 Simulated FP transmission spectrum.

Note that only the regions with positive slopes represent stable solutions that gives the possible locked laser wavelength for a given free-running operating wavelength [2, 27]. They correspond to the constructive interference between the feedback light and the laser light, while the points on the negative slope correspond to destructive interference. The curve shows a periodic structure with a period of 0.16 pm, representing the external cavity mode separation and corresponding to the FSR of the feedback loop. A close-up view of the curve around the FP transmission peak is shown in Figure 2-4 with stable solutions illustrated by red regions. Due to the long feedback loop, multiple stable states exist for a given free-running laser wavelength. For example, the blue dots represent the multiple potential optical locking points of the laser, each corresponding to an external cavity mode, for a free-running wavelength marked by the black dashed line.

We draw an additional useful conclusion from further examination of the steady-state solutions. The slope of the stable region and, consequently, the linewidth reduction, are mainly determined by the external cavity (feedback loop) length rather than the FP spectral width for a

long loop length. For a given operating point, a shift of the FP transmission peak has little effect on the locked laser wavelength.

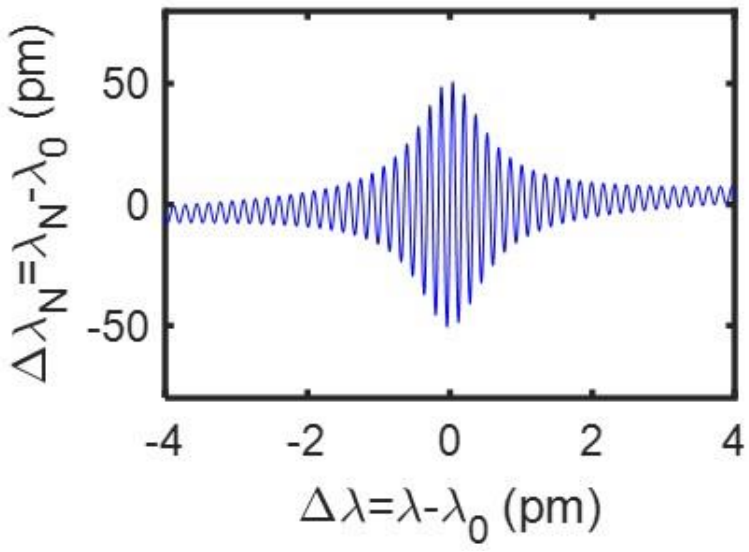

Figure 3.4 Calculated wavelength of free-running laser vs. wavelength of optically locked laser under steady state.

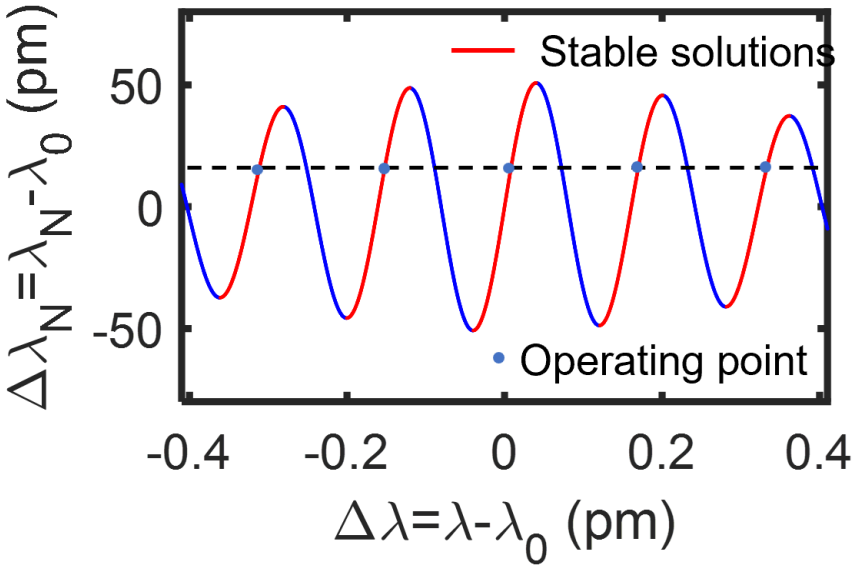

Figure 3.5 Close up view of showing stable and unstable solutions.

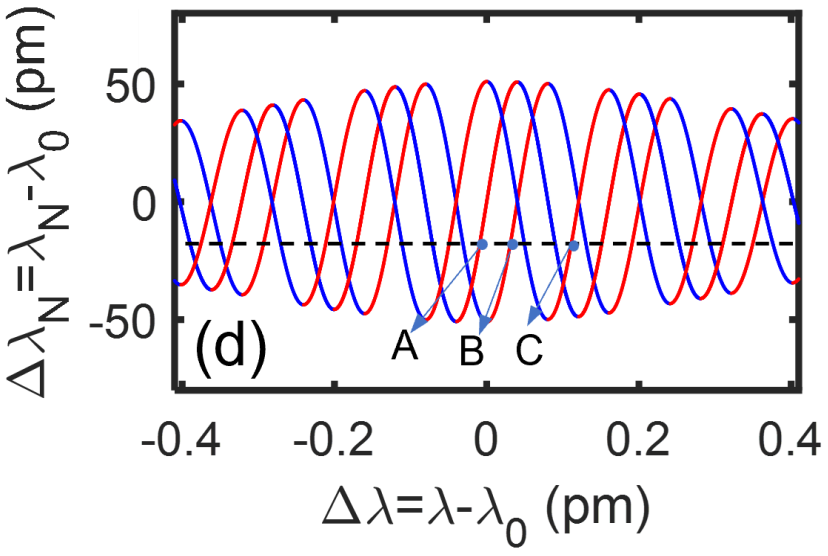

Figure 3.6 Steady-state solutions at three different phase delays of the feedback light.

The locked laser wavelength can be tuned by changing the phase delay of the feedback light through, e.g., changing the feedback loop length. This is illustrated by Figure 2-5 representing the steady-state solutions for three phase delays with curves B and C having additional phase delays of, respectively, $\pi/4$ and $3\pi/4$ with respect to curve A, by increasing the optical length of the feedback loop (nL_d) by $\lambda_0/4$ and $3\lambda_0/4$, respectively. For a constant free-running laser wavelength, the operating point shifts toward longer wavelength and shifts by approximately an FSR (0.16 pm) of the feedback loop for a phase delay change of 2π. Due to the long fiber loop length, environmental perturbations can easily change the phase delay and cause the drift of the locking wavelength.

2.3. The error signal to pin the optically locked laser wavelength to the FP transmission peak

The wavelength drift from environmental perturbations can be countered by an external feedback control system that pins the optically locked laser wavelength to the FP transmission peak. In this method, the cavity length of the FP is modulated by a weak sinusoidal signal. A portion of the light in the loop after passing the FP is coupled out and detected by a photodetector, as shown in Figure 2-1. The output from the photodetector can be used to generate an error signal that, at the vicinity of the FP peak wavelength, is proportional to the deviation of locked laser wavelength from the unmodulated FP peak wavelength. This error signal is then fed into an optical fiber stretcher to control the phase delay of the feedback light and pin the locked laser wavelength to the unmodulated FP peak, which stabilizes the optically locked laser wavelength.

The details of the error signal generation are illustrated by Figure 2-6. The FP cavity-length modulation results in a sinusoidal oscillation of the FP transmission spectrum. The FP spectral oscillation does not lead to any significant changes to the locked laser wavelength as it is determined by the phase delay of the feedback light which is insensitive to the small FP cavity length changes due to the long fiber loop. As a result, the ac component of the output of the photodetector is proportional to the slope of the FP spectrum and its phase relative to the modulation signal tells if the laser wavelength is on the side with positive or negative slope. Figure 2-6 sketches the output of the photodetector corresponding to three operating points, A, B, and C, at the vicinity of FP peak and corresponding PD outputs with respective the modulation signal.

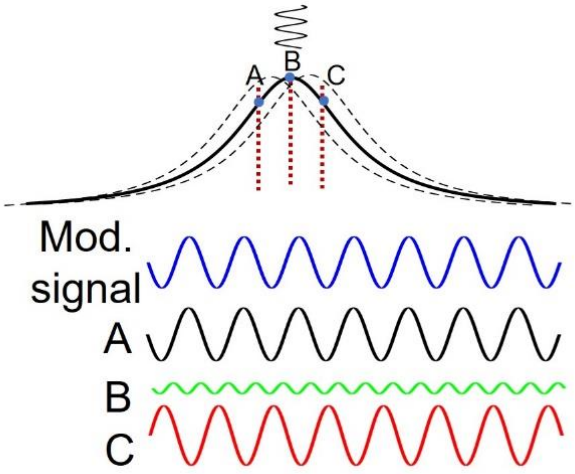

Figure 3.7 Schematic of photodetector output in response to the modulation signal for three operating points on the FP spectrum.

They are located on the positive slope (A), the peak (B), and the negative slope (C) on the FP spectrum. It shows that the amplitude and the phase of the fundamental frequency component of the output from the photodetector tells the deviation amplitude and direction of the operating point relative to the FP peak and can be used as the error signal to control the fiber stretcher and pin the optically locked laser wavelength to the FP peak.

A simple model is used to illustrate the specific operation to generate the error signal. The FP transmission spectrum can be approximated by a parabolic function at the vicinity of the peak. For a wavelength deviation of $\Delta\lambda$ between the locked laser and the FP peak, the photodetector output can be written as

$$T(\Delta\lambda, t)=k_1(\Delta\lambda+\Delta\lambda_0 \cos\Omega t)^2+k_0, \tag{2.9}$$

where $\Delta\lambda_0$ and Ω are, respectively, the amplitude and the frequency of the FP spectrum modulation, and k_1 and k_0 are two constants related to the spectral shape of the FP transmission.

The fundamental frequency component of the output can be extracted by multiplying the output with the modulation frequency followed by a low-pass filter (LPF):

$$e(\Delta\lambda)\sim LPF[T(\Delta\lambda, t)\cos\Omega t]=k_1\Delta\lambda_0\Delta\lambda, \quad (2.10)$$

which is linearly proportional to the deviation of the optically locked laser wavelength from the FP peak wavelength. Therefore, $e(\Delta\lambda)$ can be used as the error signal to control the fiber loop length for maintaining the wavelength at the unmodulated FP peak. The analysis only applies to the vicinity of the FP peak where parabolic approximation is applicable.

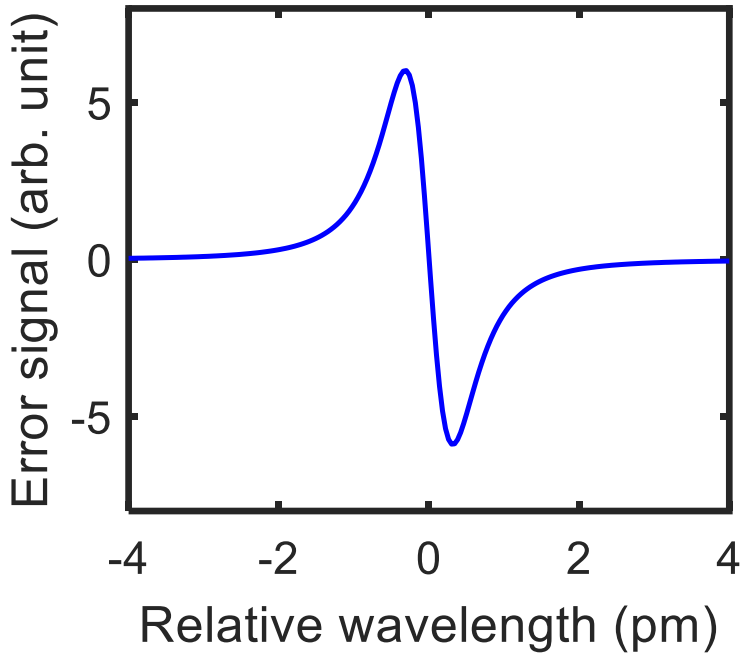

Figure 3.8 Simulated error signal vs. laser wavelength relative to FP peak.

Figure 2-7 plots the simulated error signal obtained from Eq. (2.10) for the same FP shown in Figure 2-2. The locking range is the region with negative slope around the center.

Chapter 3: Demonstration of Phase Delay Control Using Self Injection Locked Setup

Part of the material in this chapter has been published in “A. Mitul and M. Han*, "Wavelength drift suppression of semiconductor laser with filtered optical feedback from fiber-optic loop using active phase-delay control," Optics Letters, 47, 5457-5460 (2022).

3.1. Experimental setup to control phase delay and suppress wavelength drift

We demonstrated the proposed scheme experimentally using a setup schematically shown in Figure 3-1. The configuration is similar to the one shown in Figure 2-1(a). Here, we only highlight a few important differences and the details pertinent to the operation.

The light source was a customized 1550 nm DFB diode laser without a built-in isolator. The DFB output was coupled to the slow axis of the polarization-maintaining (PM) fiber pigtail, then injected into a fiber ring through a PM fiber circulator. The FP is formed by two identical 3-mm long uniform fiber-Bragg gratings (FBGs) separated by 4-mm long section of unperturbed optical fiber. The spectrum of the transmission peak for optical locking is shown in Figure 3-2, which has a FWHM of ~1.8 pm.

It was mounted on a 2-cm long piezoelectric stack driven by a function generator for modulating the FP peak wavelength. Part of the fiber in the loop was glued on an aluminum plate in a cantilever beam configuration with the free end of the cantilever beam mounted on a motorized translation stage and controlled by a computer. A polarization beam-splitter (PBS) and a polarization controller (PC) were also included in the ring to tune the feedback light polarization aligned with the slow axis of the PM fiber to ensure coherent optical feedback. Note that fibers in the ring between the PM circulator and the PBS were regular single-mode fibers rather than PM fibers. The overall fiber length of the feedback loop is estimated to be slightly longer than 20 m, resulting an

external cavity mode spacing of ~10 MHz (0.08 pm). The feedback power factor was estimated to be -15dB. The modulation signal that drove the piezoelectric actuator for modulating the FBG-FP spectrum had frequency of 100 Hz and a peak-to-peak voltage of 20 mV, resulting in wavelength shift of 0.1 pm for the FBG-FPI, which is slightly larger than the external mode spacing (0.08 pm).

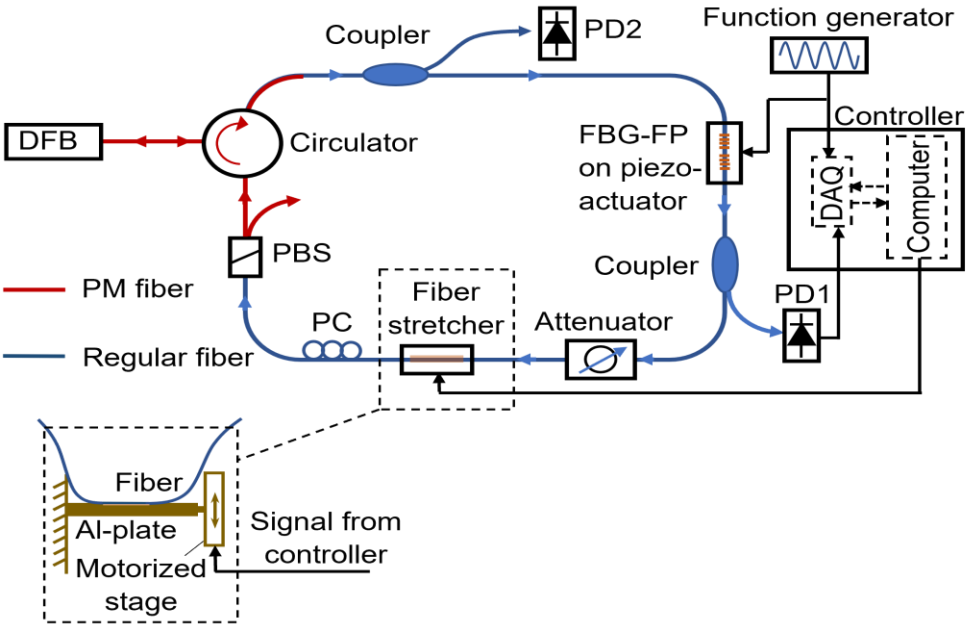

Figure 3.1 Schematic of the experimental set up.

A data-acquisition (DAQ) device with a sample rate of 2.5 ks/s was used to record the modulation signal, the photodetector (PD1) output after the FP, and the output from another photodetector (PD2) for monitoring the light power before the FP. Through the DAQ, the computer continuously recording the data in frames of 500 data points (20 ms). For each frame, the computer performs the operation described in Eq. (2.10) to obtain the error signal and move the motorized translation stage accordingly to control the feedback light phase delay.

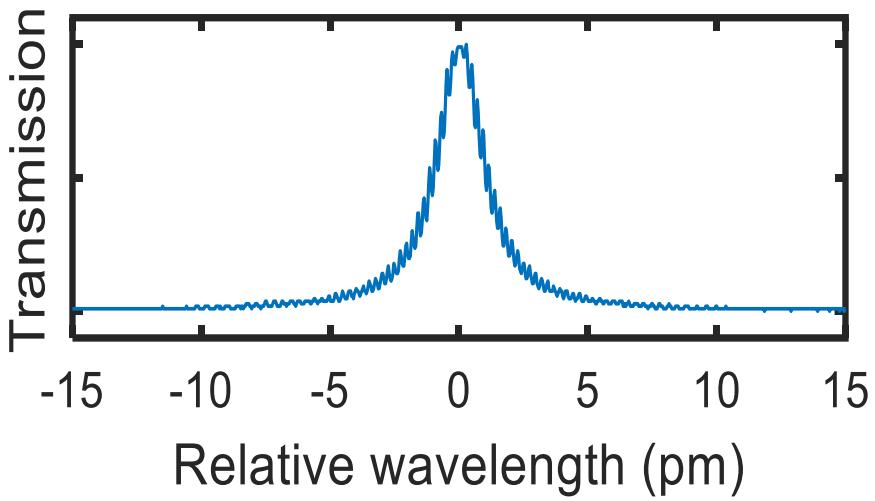

Figure 3.2 Measured transmission spectrum of the FBG-FP.

3.2. Phase delay control mechanism using self-injection locked setup

Before activating the system for the phase delay control, we observed the PD1 output for different phase delays of the feedback light by manually bending the cantilever beam with the fiber. We found that the PD1 output a sinusoidal signal in response to the modulation, which was either in phase or out of phase relative to the modulation signal. The phase relationship and the amplitude of the PD1 output could be controlled by tuning the phase delay. For example, Figure 3-3, Figure 3-4, Figure 3-5 show PD1 output and the corresponding modulation signal when the operating point was on the positive slope of the FBG-FP transmission spectrum with PD1 giving an in-phase response [Figure 3-3], at the peak with the signal dominated by a double frequency component [Figure 3-4], and on the negative slope with PD1 giving an out-of-phase response [Figure 3-5]. These results are consistent with the prediction shown in Figure 2-6. Note that we found the laser output power, detected by PD2, remained unchanged as the phase delay was tuned.

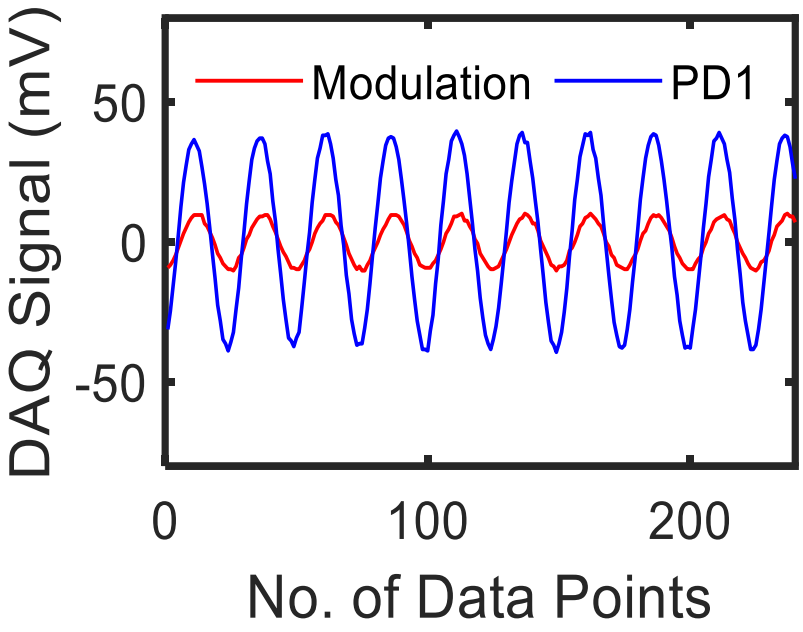

Figure 3.3 PD1 output in phase relative to the modulation signal.

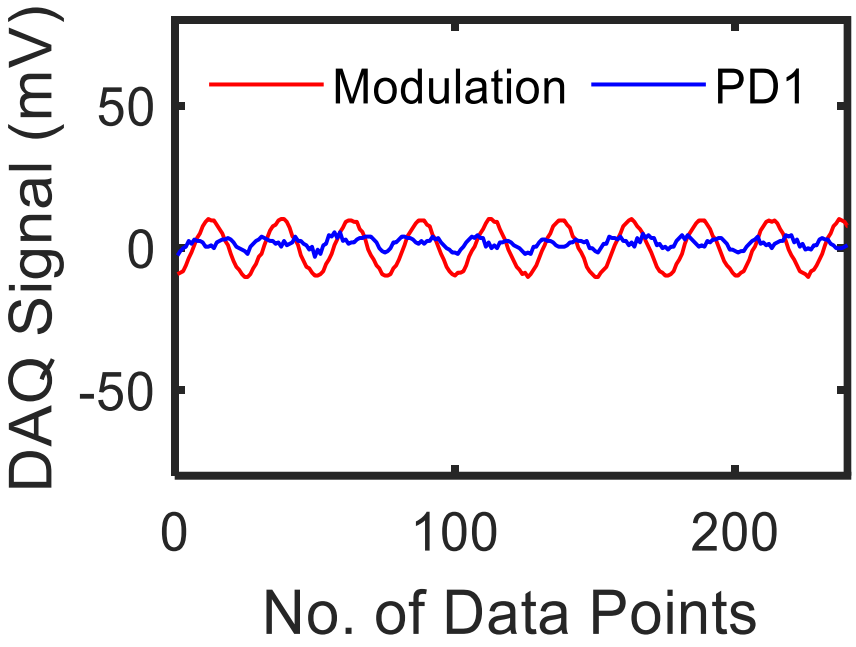

Figure 3.4 Double frequency component in PD1 output.

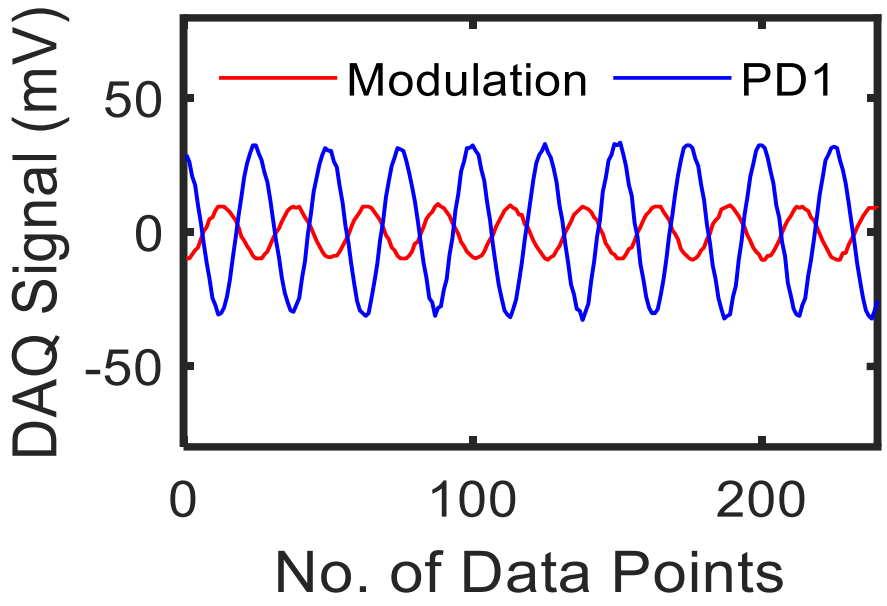

Figure 3.5 PD1 output out of phase relative to the modulation signal.

3.3. Experimental result w/ and w/o utilization of phase delay control

Then we activated the control system for the feedback light phase delay. To simulate the relatively large phase delay from the fiber-optic loop over long term, part of the fiber in the loop was manually and slowly stretched in a random way. Figure 3-6 and Figure 3-7 show, respectively, the evolution of the PD1 output and the error signal during a period of 130 s. For comparison, the results when the phase delay control was deactivated are also presented. The phase delay control resulted in less variations of both the PD1 output and the error signal, indicating a more stable laser wavelength relative to the FBG-FP peak.

Figure 3-8 plots the PD1 output vs. the error signal that provides a more straightforward way to visualize the laser wavelength changes.

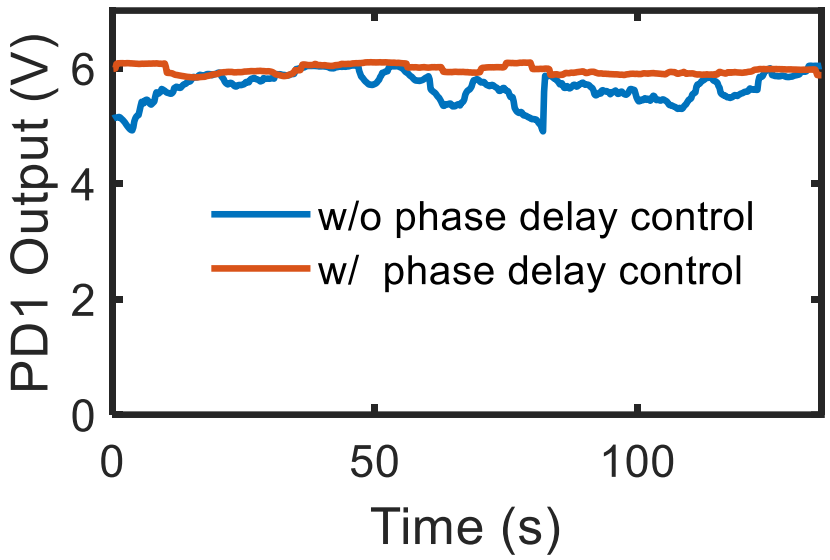

Figure 3.6 Time evolution of PD1 output.

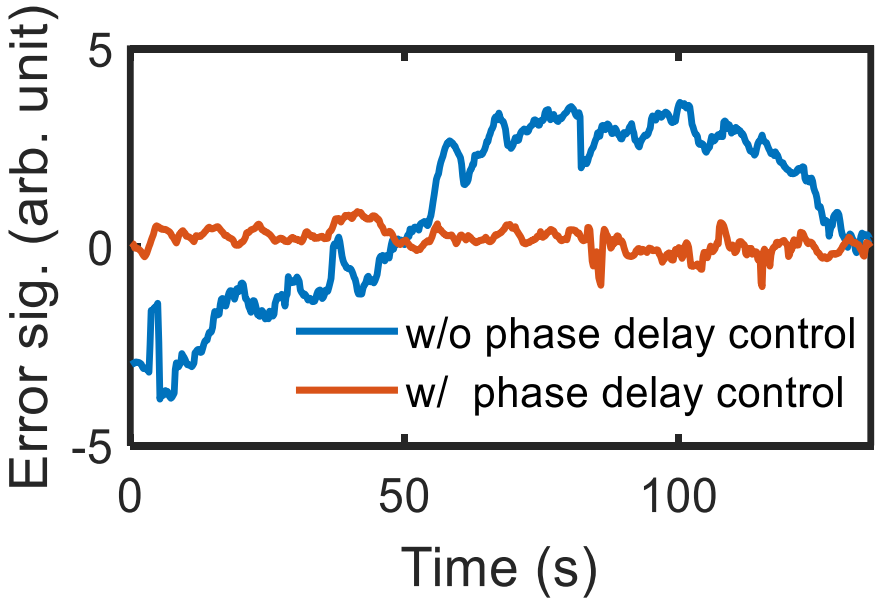

Figure 3.7 Time evolution of the error signal.

In theory, this plot resembles the transmission spectrum of the FBG-FP over the range of the laser wavelength shift as the error signal is proportional to the laser wavelength deviation from the FBG-FP peak at the vicinity of the peak [see Eq. (2.10)]. For the case of no phase delay control, the results show a general agreement with the spectral shape of the FBG-FP which can be

approximated by a parabolic function around the peak [see Eq. (2.9)]. With the phase delay control, the laser wavelength was confined to a much smaller range around the center. From the results, we estimate that the wavelength drift was reduced by ~75% with the phase delay control compared to the case without phase delay control. We note that there were variations in the PD1 output for a given value of error signal. Interestingly, Figure 3-8 seems to suggest a pattern of several individual parabolic curves stacked together. This may be caused by some composite interferometers in the fiber loop that modified the overall spectral shape of the feedback. During the perturbation to the fiber loop, mode hopping occurred that led to different patterns for the PD1 output vs. error signal.

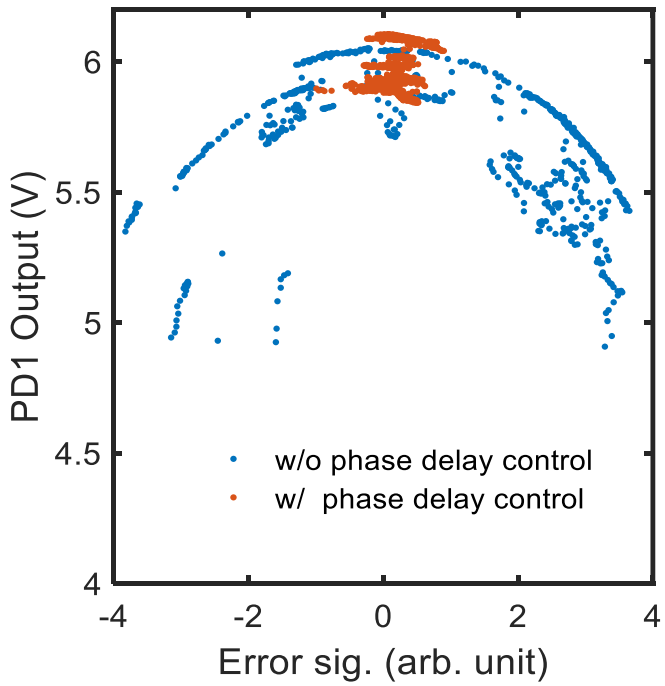

Figure 3.8 PD1 output vs. error signal.

3.4. Linewidth measurement: Delayed self-heterodyne technique

Finally, we measured the linewidth of the lasers using the delayed self-heterodyne technique using a fiber-based unbalanced Mach-Zehnder interferometer with a 40 km fiber delay line and a 100 MHz acousto-optic modulator as shown in Figure 3-9.

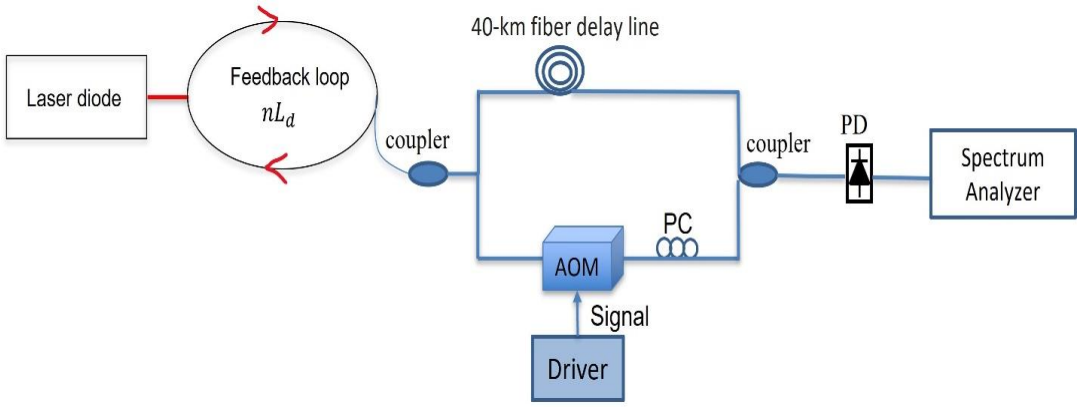

Figure 3.9 Delayed self-heterodyne technique.

The beat note spectra were measured by an electronic spectrum analyzer with its resolution bandwidth set to be 1 kHz and the results are shown in Figure 3-10. The beat note of the free-running laser shows a 20-dB width of ~350 kHz. Optically locking greatly reduces the linewidth and there were no significant differences in the beat note spectra between the cases with and without active phase delay control. Detailed beat note spectra for the optically locked laser [Figure 3-11] shows a 20-dB bandwidth of ~10 kHz. Note that the spectra show sidelobes with a frequency interval of ~5 kHz, equal to the reciprocal of the time delay from the 40 km fiber. It suggests that the coherent length of the optically locked laser may exceed the optical length of the optical fiber delay line, which makes it difficult to determine the true linewidth of the optically locked laser using the current delayed self-heterodyne configuration.

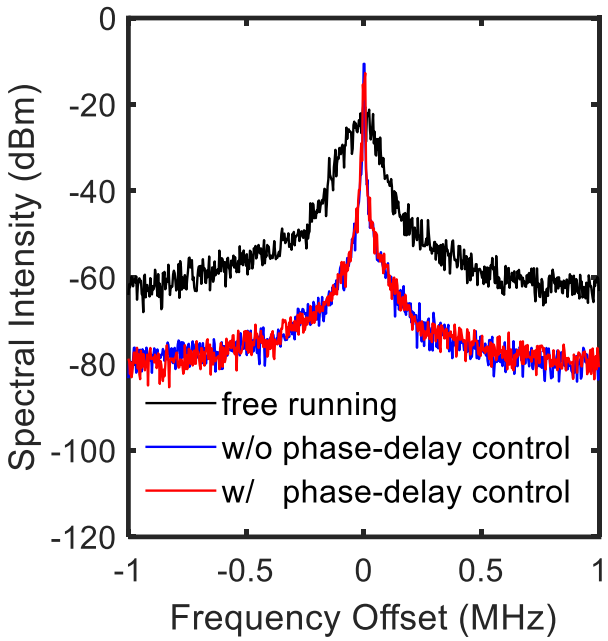

Figure 3.10 Power spectra of the beat note signal with its resolution bandwidth set to be 1 kHz.

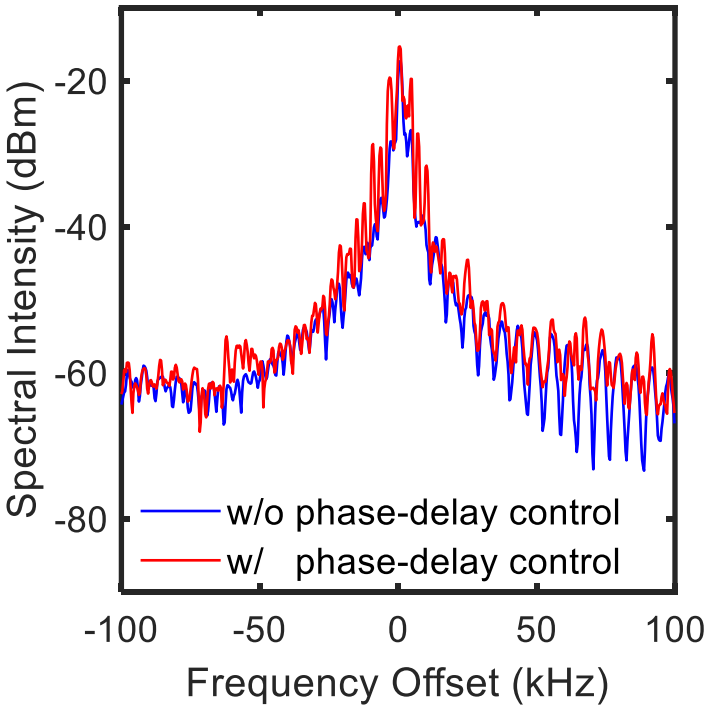

Figure 3.11 Detailed beat note spectra for the optically locked laser.

Chapter 4: Characterization of Mode-Hopping and Laser Frequency oscillations in Self-Injection Locked Laser

Part of the material in this chapter has been published in "K. Farzim, A. Mitul, B. Zhou, and M. Han*, "High-sensitivity demodulation of fiber-optic acoustic emission sensor using self-injection locked diode laser," IEEE Photonics Journal, 14, 7142610 (2022).

4.1. Self-Injection Locked DFB Diode Laser

The self-injection locked DFB diode laser is similar to the one described in [82] and is schematically shown in Figure 4-1. The light source is a DFB diode laser without an integrated isolator at ~1545 nm. The optical feedback path included the fiber pigtail of the DFB laser and a fiber loop. The light from the DFB laser was coupled to the fiber loop through a circulator and traveled through a high-finesse FBG-FPI functioning as the locking resonator before it was injected back to the laser diode through the same circulator. Other components included in the fiber loop were a polarization controller (PC) for aligning the laser polarization with one of the principal axes of the FBG-FPI, an attenuator for adjusting the feedback coefficient, and two fiber-optic couplers. The feedback level needs to be adjusted to an appropriate level. It should be large enough to the induced locking. We also found that too much feedback tends to induce more frequent episodes of laser instability. The 33:67 coupler before the PC was used to couple out a portion of the light in the cavity as the output of the self-injection locked laser that would be sent to the fiber-optic AE sensor system. The 50:50 coupler after the FBG-FPI was used for monitoring the mode-hopping events as described below. The locking resonator is an FBG-FPI consisting of two identical 3-mm long uniform FBGs at ~1545 nm separated by a 4-mm long fiber. Its transmission spectrum had several resonant peaks with the narrowest one having a 3-dB linewidth of 1.5 pm (shown in the Figure 4-2) that was used for self-injection locking.

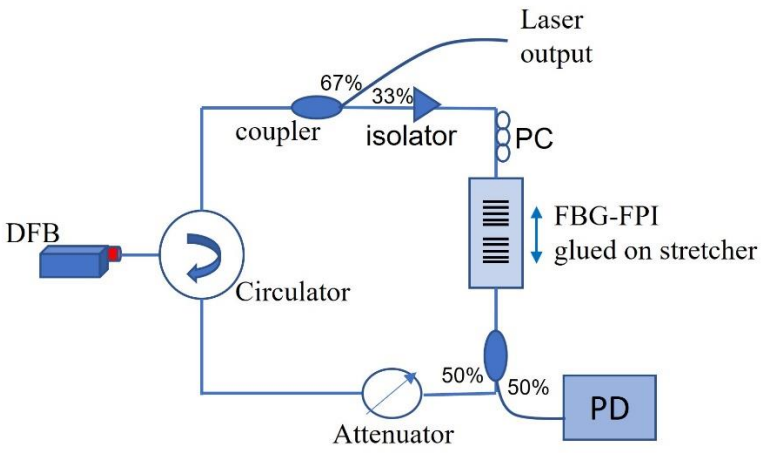

Figure 4.1 Schematic of self-injection locked DFB laser locking setup. PD: photodetector, PC: polarization controller.

The front facet of the laser diode and the feedback path including the fiber pigtail and the fiber loop formed an external cavity that was weakly coupled to the DFB laser cavity in the laser system. The feedback path length ranged from a few meters to over 20 meters by including jump cables in the fiber loop. As schematically shown in Figure 4-3, the long feedback path length results in dense external cavity modes over a broad wavelength range. When the appropriate feedback coefficient is obtained by tuning the attenuator, the laser is then locked to one of the external cavity modes around the transmission peak of the FBG-FPI. Ambient perturbations such as temperature variations and vibrations to the fiber feedback path can cause drift of the external cavity modes and changes of the relative positions of the external cavity modes and the resonator peak. For example, the thermos-optic coefficient of silica is $dn/dT = \sim 1 \times 10^{-5}$. A relative temperature change of 0.1 °C between the FPG-FPI and the fiber loop would cause a 1 pm wavelength drift between the external cavity mode and the FBG-FPI peak, which is significant considering the 1.5 pm spectral width of the FBG-FPI peak.

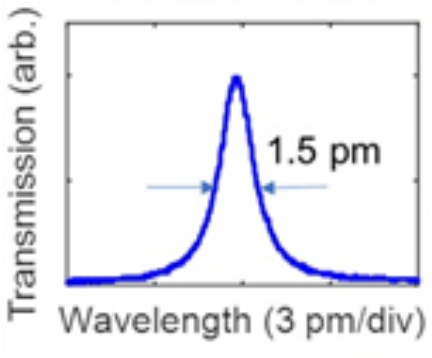

Figure 4.2 Spectrum of the transmission peak of an FBG-FPI in the feedback loop.

As schematically shown in Figure 4-4, when the external mode to which the laser is locked drifted away from the resonator peak, the optical loss of the mode-hopping increases and may eventually jump to the neighboring external cavity mode with smaller loss, resulting in a mode-hopping event. Accompanied with the mode-hopping event is an abrupt change of the light intensity after the resonator, which can be monitored by a photodetector.

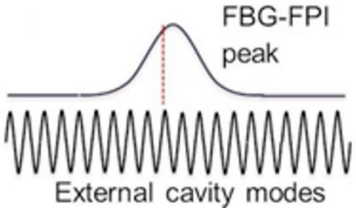

Figure 4.3 Schematic illustration of dense external cavity modes with respect to the FBG-FPI transmission spectrum.

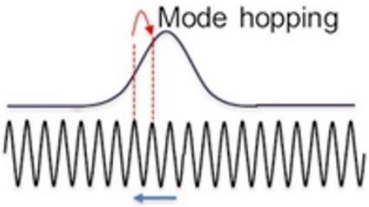

Figure 4.4 Schematic illustration of Mode-hopping event of the self-injection locked laser.

Mode-hopping does not occur frequently for the self-injection locked DFB diode laser under laboratory environment. The laser can maintain stable operation over periods ranging from a few seconds to a few minutes. The laser was locked to one of the external cavity modes close to the resonant peak of the FBG-FPI. The interval of the external cavity modes is determined by the free-spectral range (FSR) of external cavity (feedback loop) given by $\mathrm{FSR} = \lambda^2/2nL$, where λ is the wavelength of operation, n is the refractive index of the fiber, and L is the length of the feedback loop. Shorter loop length provides a larger FSR and on average, a larger change in the optical loss between neighboring external modes, resulting in less frequent mode-hopping jump with on average, larger mode-hopping jump height because of the large distance between the external cavity modes. On the other hand, longer loop provides smaller FSR with denser sinusoidal fringes resulting in more frequent mode-hopping occurs with smaller jump levels due to the smaller distance between the external cavity modes. The number of mode-hopping increases with the increasing of loop-length. On the other hand, average normalized height of mode-hopping jump decreases with the increasing of loop length and number of mode-hopping. Shorter loop lengths provided smaller number of mode-hopping events with larger jump heights. Therefore, reducing the feedback loop length can effectively reduce the number of mode-hopping events in a self-injection locked DFB diode laser. It needs to be stressed that the experiment was performed in a laboratory environment. Larger perturbations that can be experienced in the field may cause more frequent mode- hopping and even unlocking of the laser if the discrepancy between the free-running laser wavelength and the resonator wavelength becomes large. As the minimum feedback loop length may still be on the order of meters due to the use of fiber-pigtailed lasers and other fiber-pigtailed components, the laser system is expected to be prone to environmental perturbations and likely needs to be packaged and protected for practical applications in the field. Active

approaches, e.g., controlling the drift of the external cavity mode through a fiber stretcher, to minimize the mode-hopping could also be considered.

4.2. Study of mode-hopping and the instability of the self-injection locked laser

Environmental perturbations could cause a relative drift of the external cavity mode with respect to the resonator wavelength of the self-injection locked laser that leads to mode-hopping. It is expected that mode-hopping will result in a step change of laser frequency. We found that the laser wavelength is typically locked to the slope of the resonator, where the wavelength change is converted to intensity variations of the light passing through the resonator. Therefore, the occurrence of mode-hopping can be identified by monitoring the intensity of the light after it passes through the resonator in the feedback loop. We used various photodetectors to observe the signal, including a broadband dc-coupled um-amplified photodetector (Model: DET01CFC, Thorlabs) with a bandwidth from dc to 1.2 GHz to observe the overall signal and an amplified photodetector (Model: 1811, Newport) with both an ac (25 kHz-125 MHz) output and a quasi-dc (dc-50 kHz) output. As shown in Figure 4-5, the amplified photodetector was also applied to the laser output port to monitor the intensity of the light before passing through the resonator.

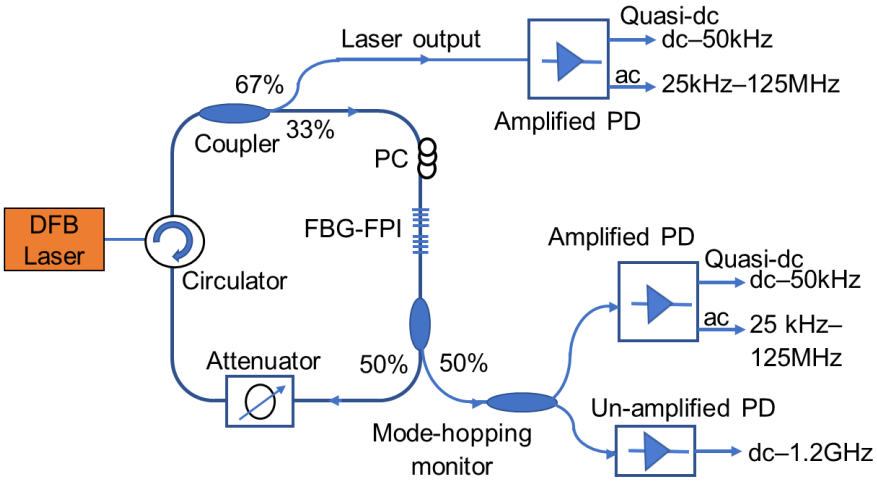

Figure 4.5 Experimental setup to study mode-hopping and the instability of the self-injection locked laser.

4.3. Experimental results of mode-hopping and the instability of the self-injection locked laser

We first studied the signals from the mode-hopping monitoring port of the laser system. Figure 4-6(a) shows the output from the un-amplified photodetector when a mode-hopping event occurred. It shows that the mode-hopping resulted in a jump in the signal level followed by unstable laser operation as indicated by the rapid variations of the output that lasted for less than 1 s. Due to the presence of the instability, it is difficult to accurately characterize the transient time of the mode-hopping. The variations are more clearly visible at the ac output of the amplified photodetector (Figure 4-6b). The quasi-dc output of the photodetector with a 50 kHz bandwidth (Figure 4-6c) only shows a step change of the output, which can be attributed to the mode-hopping, but is absent of the variations associated with the laser instability, indicating that the variations have no frequency components below at least 50 kHz. Figure 4-6(d) shows the details of the variations at another instance when the laser instability was observed. It indicates that the variations have a periodic structure with a period of 86 ns, corresponding to a fundamental frequency of ~11 MHz. We found that the period of the oscillations corresponds to the time delay of the feedback light. Note that, the shape of the oscillations may deviate from a sinusoidal shape. In those cases, the signal may contain strong components at higher-order harmonic frequencies.

For the case shown in Figure 4-6, the laser become unstable following the mode-hopping. We also observed that the instabilities can precede the mode-hopping or occur spontaneously without mode-hopping. For example, in Figure 4-7(a), a mode-hopping event indicated by the step change in the quasi-dc output of the amplified photodetector is preceded by the variations indicative of the laser instability recorded from the ac port of the amplified photodetector.

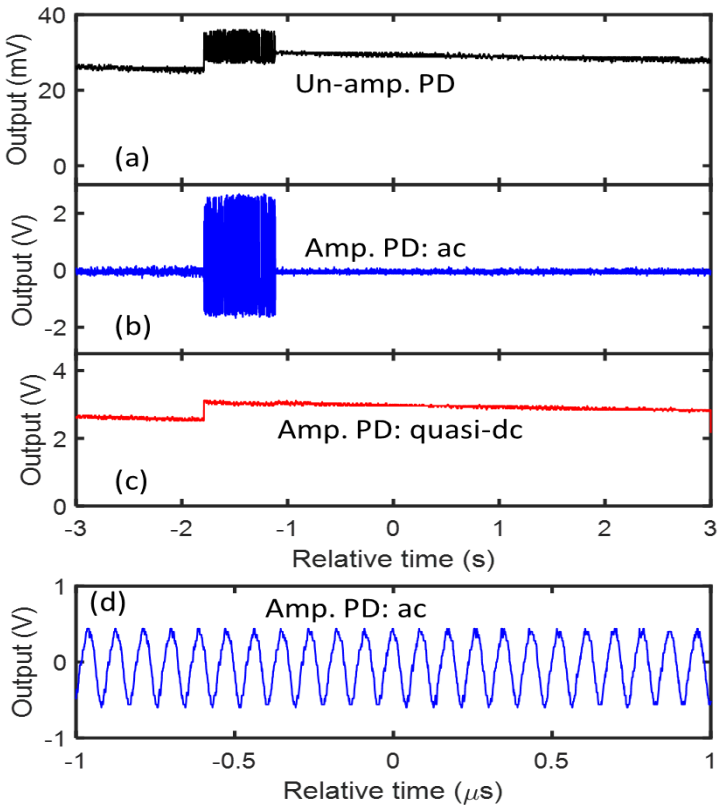

Figure 4.6 (a-c) Signals from the photodetectors (PDs) connected to the mode-hopping port of the self-injection locked laser. (d) Oscillation signals from the ac output of the amplified PD when the laser is in unstable operation.

In another example shown in Figure 4-7(b), the quasi-dc output has no step changes, indicating the absence of mode-hopping. However, the laser instability is clearly shown in ac output. We note that, the laser instability lasted for various length of the order of seconds.

The variations recorded by the photodetectors were caused by the laser frequency oscillations rather than the laser intensity variations at the output of the locked DFB laser. It is proved by the experiment of simultaneously monitoring the output from the mode-hopping port (laser intensity after the resonator) and the laser output port (laser intensity before the resonator) as shown in Figure 4-5.

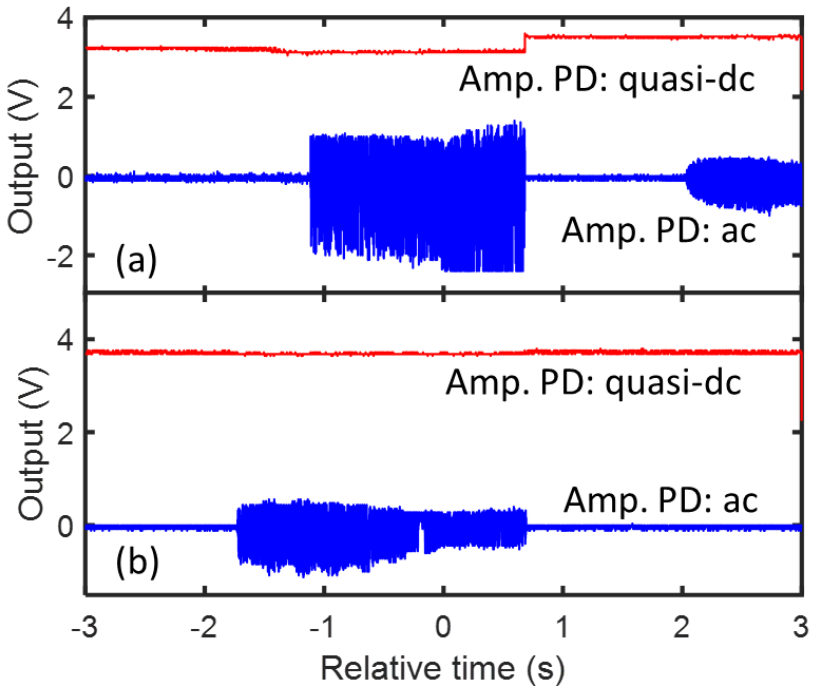

Figure 4.7 (a) and (b) are the two instances in which the laser instability (a) occurs preceding the mode-hopping and (b) occurs spontaneously without mode- hopping.

The results are shown in Figure 4-8, where Figure 4-8(a) is the ac output of the amplified photodetector at the mode-hopping monitoring port and Figure 4-8(b) and (c) are respectively the quasi-dc and ac outputs of another amplified photodetector at the laser output port. Figure 4-8(a) shows that the laser operation was unstable before relative time t≈0.8 s and became stable afterwards. Between these two laser states, no changes were observed in either the quasi-dc output or the ac output for the laser output ports. Therefore, the variations observed in Figure 4-8(a) must have come from the laser frequency variations that were converted to the laser intensity variations at the spectral slope of the resonator. Similar frequency oscillations have also been observed in self-injection locked semiconductor lasers with long free-space coupled feedback loops [3, 29] .

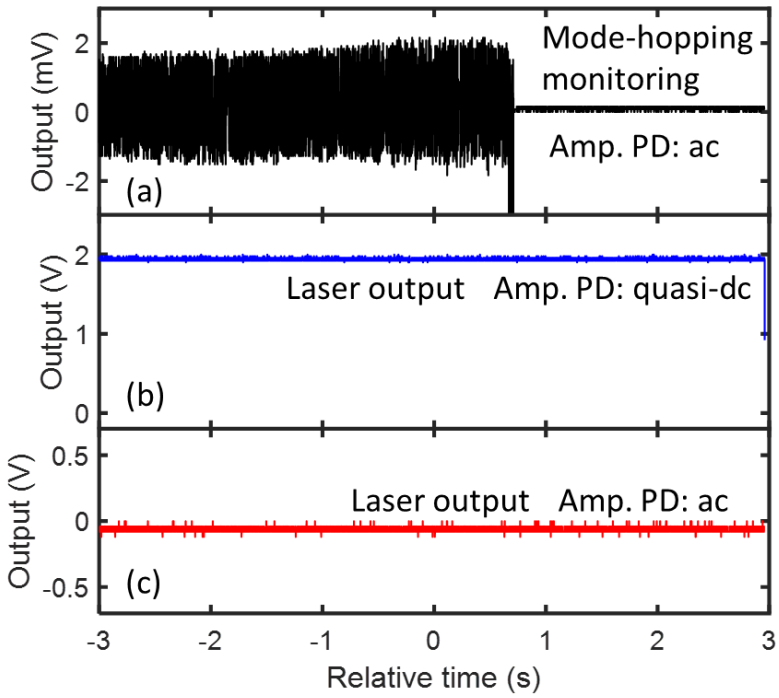

Figure 4.8 (a) Instability recorded from amplified PD connected to mode-hopping monitoring port of self-injection locked laser after resonator. (b-c) are signals from the amplified PDs connected to the laser output port before resonator.

We measured and compared the electronic spectrum of the signal from the ac output of the amplified photodetector connected to the mode-hopping monitoring port when the self-injection locked laser was in stable state and unstable state. Figure 4-9 shows an example of the measured spectra. It verifies the conclusions from the time-domain analysis. The laser under stable state shows a flat baseline in the bandwidth of the detector. The unstable operation of the laser results in oscillations with a fundamental frequency of ~11 MHz. Several strong harmonic frequency components also show up. However, the noise level remained unchanged between the stable and unstable operation for frequencies other than at these discrete values.

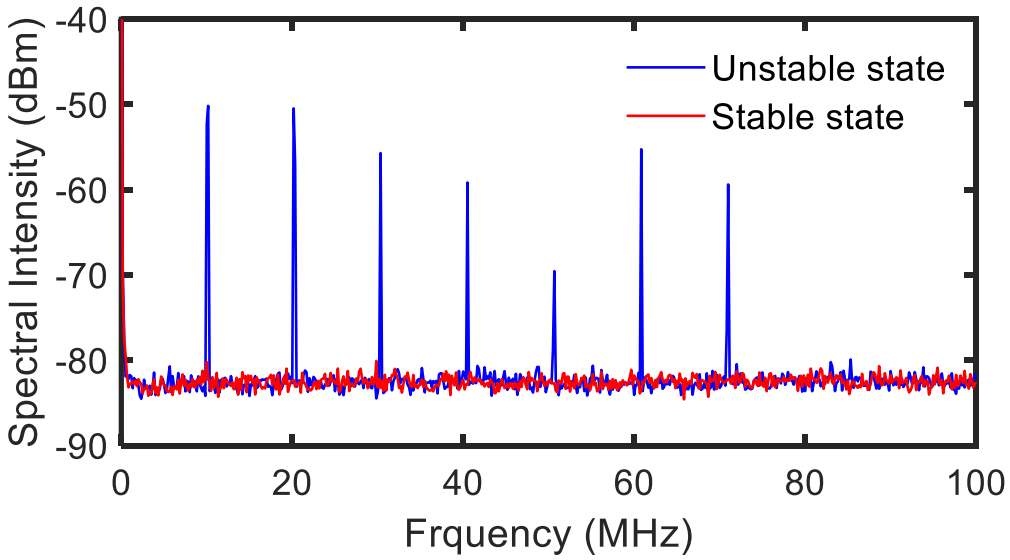

Figure 4.9 Spectra of the signals from the ac output of the amplified PD connected to the mode-hopping monitoring port when the laser is in unstable operation (blue) and in stable operation (red).

Finally, we note that, due to the presence of the instability and the short time scale of the dynamics, it is difficult to accurately capture the temporal evolution as the locked laser frequency jumps from one mode to the other mode during a mode-hopping event. Relaxation oscillation (RO) is involved in establishing a lasing mode in the process. The RO frequency of a DFB laser typically is > 1 GHz.

Chapter 5: High-Sensitivity Demodulation of Fiber-Optic Acoustic Emission Sensor Using Self-Injection Locked Diode Laser

Part of the material in this chapter has been published in "K. Farzim, A. Mitul, B. Zhou, and M. Han*, "High-sensitivity demodulation of fiber-optic acoustic emission sensor using self-injection locked diode laser," IEEE Photonics Journal, 14, 7142610 (2022).

In this chapter, we demonstrate the use of a self-injection locked DFB diode laser for high-sensitivity demodulation of a fiber-coil FPI AE sensor formed by two weak FBGs on the ends of a long span of coiled fiber [84]. Taking advantage of the dense sinusoidal fringes of the sensor reflection spectrum, we developed a modified phase-generated carrier (PGC) demodulation method that does not require agile tuning capability of the laser [85]. Experimental results indicate that, compared with the free running DFB laser, the self-injection locked laser increases the signal-to-noise ratio (SNR) by ~33 dB compared with that of the free-running DFB laser. We also studied the effect of the mode-hopping events of the self-injection locked laser on the demodulated signal. We found that mode-hopping is often associated with laser frequency oscillations that could last for a length of the order of seconds. The mode-hopping event causes an abrupt change in the laser intensity after the resonator inside the feedback loop. It manifests itself as a short transient signal in the output of the AE sensor system. With the identification of the mode-hopping events, the associated spurious signal can be identified and discarded in the signal processing without causing significant disruption to the sensor system. We also found that laser frequency oscillation can also occur spontaneously without the mode-hopping. The spectrum of the laser frequency oscillations shows narrow peaks at the fundamental frequency determined by the feedback loop length and its harmonics. Because these frequency components are much higher than the bandwidth of the fiber-

optic AE sensor system, they have no effect on the performance of the sensor system. Finally, we show that the frequency of mode-hopping is highly related to the length of the feedback loop and reducing the loop length can effectively reduce the frequency of mode-hopping.

5.1. Fiber-Optic AE Sensor and Modified PGC Demodulation

We demonstrated the application of self-injection locked laser for AE detection using a low-finesse FPI sensor demodulated by a modified PGC method [85]. The sensor was made from a pair of weak FBGs at the ends of a fiber coil made from a span of ~40-cm long optical fiber, leading to approximately sinusoidal fringes with a free-spectral range of ~2 pm and the fringe profile determined by the FBG reflection spectrum. The outer and inner loop diameter of the fiber coil sensor was 10 mm and 8 mm, respectively. The schematic of the fiber-coil sensor and its reflection spectrum, as well as the measured fine fringes of the sensor, are shown in Figure 5-1(a). Details on the fabrication and characterization of the sensor can be found in [84]. As shown in Figure 5-1(b), the coiled region of the sensor was then glued on an aluminum plate (91 cm × 66 cm × 1 mm) for testing. AE signals were simulated by a piezo transducer glued on the aluminum plate around 2 cm away from the center of fiber coil sensor which was driven by a sinusoidal signal of 150 kHz, 10 V peak-to-peak, 4 cycle burst (10 ms period) from a function generator. Since only the coiled fiber region (without FBGs) was bonded on the surface of a structure, surface strain including that caused by the AE signal induced changes to the phase of the sensor fringes and the spectral profile of the fringes remained unchanged.

The modified PGC method allowed to extract the AE signal encoded as the phase modulation with good linearity and high sensitivity and regardless of the laser wavelength with respect to the sensor fringes. Detailed description of the demodulation method is described in [85]. For convenience, the method is briefly introduced here. The light intensity reflected from the low-

finesse FPI may be written as $I = A + B\cos[\phi_0 + \Delta\phi(t)]$, where A and B are constants related to the laser power and the fringe visibility, ϕ_0 is a quasi-static phase term including the laser wavelength drift and environmental effect, and $\Delta\phi(t)$ is an ac term proportional to the AE signal being detected. As shown in Figure 5-1(a), the phase of the laser is modulated with a sinusoidal function with a frequency of Ω using an electro-optic phase modulator to generate the carrier signals. The light intensity reflected from the sensor, detected by a photodetector, then contains an in-phase signal, $\cos[\phi_0 + \Delta\phi(t)]$ and a quadrature signal, $\sin[\phi_0 + \Delta\phi(t)]$, modulated by carrier signals with frequencies of the even and odd multiples of Ω, respectively. The terms at carrier frequencies Ω and 2Ω, or $-2BJ_1(C)\sin[\phi_0 + \Delta\phi(t)]$ and $-2BJ_2(C)\cos[\phi_0 + \Delta\phi(t)]$, where J_1 and J_2 are, respectively, the first and second-order Bessel function of the first kind and C is a constant related to the phase modulation depth and the modulation frequency which can be obtained by mixing the output from the photodetector with sinusoidal signals at the same frequency and applying a low pass filter with a bandwidth covering the highest frequency of signal of interest. Recognizing AE-induced phase changes are small or $\Delta\phi(t) \ll 1$, we can apply the following approximations and break the in-phase and quadrature signals each into a quasi-dc component and an ac component that is linearly proportional to $\Delta\phi(t)$:

$$\sin[\phi_0+\Delta\phi(t)] \approx \sin\phi_0 + \cos\phi_0\,\Delta\phi(t)$$
$$\text{and } \cos[\phi_0+\Delta\phi(t)] \approx \cos\phi_0 - \sin\phi_0\,\Delta\phi(t).$$

The dc components can be obtained by applying a low-pass filter and ac components can be separated by a bandpass filter and an amplifier. Then we obtain the following four signals:

$$I_{1d}(t) = -2BJ_1(C)\sin\phi_0 \quad (5.1a)$$
$$I_{1a}(t) = -2BGJ_1(C)\cos\phi_0\,\Delta\phi(t) \quad (5.1b)$$
$$I_{2d}(t) = -2BJ_2(C)\cos\phi_0 \quad (5.1c)$$
$$I_{2a}(t) = 2BGJ_2(C)\sin\phi_0\,\Delta\phi(t) \quad (5.1d)$$

where G is the gain of the amplifier. Then $\Delta\phi(t)$, with the AE signal encoded in it, can be extracted with good linearity and independent on ϕ_0 through the following algebraic operation:

$$I_{1a}(t)I_{2d}(t)-I_{1d}(t)I_{2a}(t)=4GB^2J_1(C)J_2(C)\Delta\phi(t). \quad (5.2)$$

In our experiment, the phase modulator was a high-speed (10 GHz) lithium niobate electro-optic phase modulator (Model: 2942, Covega), driven by a 130 MHz sinusoidal waveform generated from a function generator and an RF amplifier. The terms at the carrier frequencies were then obtained by properly mixing the output of PD with sinusoidal waves at the fundamental and second-order harmonic of the carrier signal and a 500 kHz low pass filter (LPF). After the low-pass filter, the signal of interest, which was ultrasound, was then separated and amplified by a 40 dB amplifier and bandpass filter in the frequency range of 50-500 kHz. The bandwidth was selected to cover most of the frequency components of AE signals for crack detection in structural health monitoring applications. For quasi-DC channels, another 25 kHz LPF was applied following the 500 kHz LPF. The cut-off frequency of quasi-dc channel needs to cover the frequency range of the unwanted signals that can cause the shift of the operating point such as environmental perturbations. The four signals (2 quasi-DC and 2 AC) as represented by Eqs. (5.1a) – (5.1d) were then recorded by an oscilloscope or a data acquisition (DAQ) with a sampling rate of 2 MS/s for storage in a computer, where the operation in Eq. (5.2) was performed to obtain the output of the system. We verified that the demodulation setup could generate the in-phase and quadrature signals using the carrier signal. For this purpose, we employed a tunable laser whose wavelength was modulated by a triangular wave and recorded two quasi-DC terms, I_{1d}, I_{2d} as shown in Figure 5-1(c), which shows the system produced two sinusoidal waveforms with quadrature phase relationship.

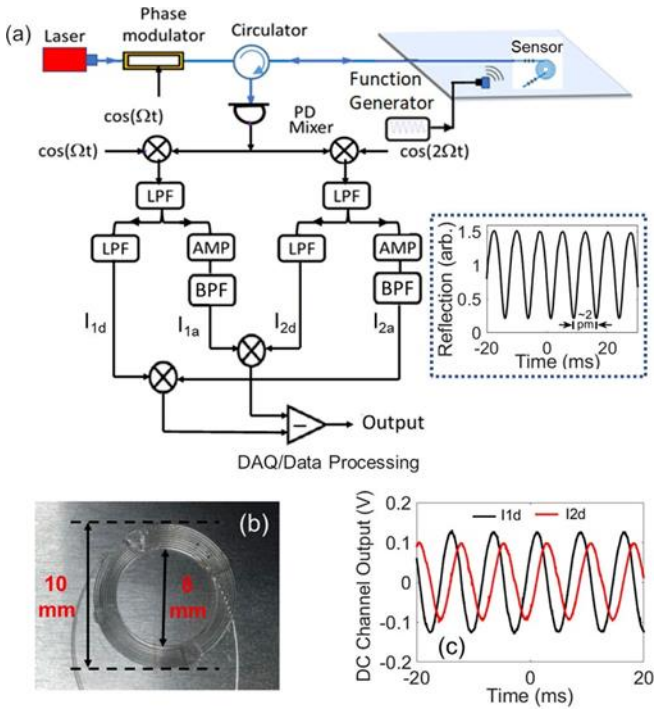

Figure 5.1 (a) Schematic of a modified PGC demodulation method for fiber coil sensor. PD: photodetector, AMP: amplifier, DAQ: data acquisition, LPF: low pass filter, BPF: band pass filter. Inset: reflection spectrum of fiber-coil sensor measured by a wavelength-scanning laser. (b) An image of a fiber coil sensor installed on an aluminum plate. (c) Two DC channel outputs while the laser wavelength was scanned linearly with time.

5.2. Comparison of SNRs with Self-Injection Locked Laser and Free-Running Laser

We connected the DFB sensor system in self injection-locked mode and in free-running mode to the demodulation system. The feedback loop length of the self-injection locked laser was approximately 9 m. The responses of both configurations to the simulated AE signal generated by the piezo transducer on the aluminum plate are shown in Figure 5-2(a) and Figure 5-2(c), respectively. It shows that both configurations yield similar overall ultrasonic response with similar peak-to-peak values around $V_{pp} = 0.43$ V². It also clearly demonstrates that; the self-injection locked mode provides much smaller noise as compared to the free-running mode of DFB laser. The noise with the free-running DFB laser is dominated by the laser frequency noise of the laser [86]. The sensor system cannot distinguish between the laser frequency variations and the

AE-induced wavelength shift of the sensor. To characterize the noise performance of the sensor system more accurately in these two configurations, we turned off the piezo transducer so that there was no simulated AE signal, and the system outputs absent of the AE signal for the self-injection locked mode and the free-running mode of DFB laser are shown in Figure 5-2(b) and Figure 5-2(d), respectively. The standard deviations of noises are 9.0×10^{-4} V^2 and 4.3×10^{-2} V^2, respectively, for these two modes. Using the peak-to-peak response and standard deviations for calculating the SNR, we found that the self-injection-locked DFB laser (SNR = 53.6 dB) provides a much better SNR which is ~33 dB larger than that the of free-running DFB laser (SNR = 20.0 dB).

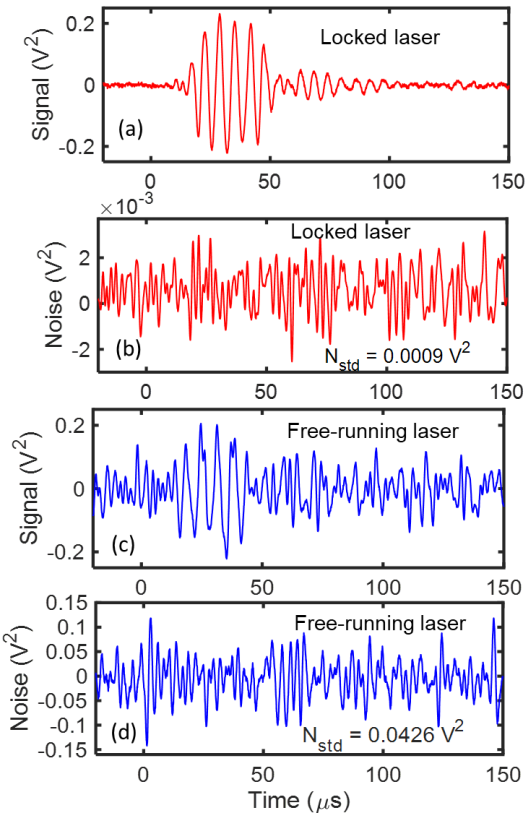

Figure 5.2 (a) Ultrasonic response and (b) noise provided by the system with self-injection locked DFB laser system. (c) ultrasonic response and (d) system noise with the same laser in free-running mode.

We also characterized the noise improvement for self-injection locked lasers with different feedback loop length in comparison to free-running laser. A longer feedback loop may further reduce the laser frequency noise [87]. However, in the current system, the noise with the self-injection locked laser was dominated by the noise from the photodetectors and the electronics of the sensor system. We found that increasing the loop length to 14 m did not cause significant changes to the SNR performance.

5.3. Effect of Mode-Hopping of Self-Injection Locked Laser on System Response

In the laboratory environment, we observed that mode- hopping occurred infrequently. To study the effect of mode hopping on the system response, we intentionally perturbed the fiber loop by bringing an incandescent light close to the FBG-FPI region to slightly heat the fiber loop, which led to more frequent mode-hopping events. The four channels in the demodulation system, I_{1d}, I_{2d}, I_{1c}, I_{2c}, as shown in Figure 5-1(a) as well as the mode-hopping monitor signal were continuously recorded. In the meantime, simulated AE signals were continuously generated with a repetition rate of 100 Hz during the data acquisition process.

Figure 5-3(a) shows the evolution of the recorded signals as well as the calculated AE response according to Eq. (5.2) over a period of ~1.5 s. Noted that, proper multiplication factor and the offset values are added in Figure 5-3 for the clarity of the curves shown in the figure. The mode-hopping events are indicated by the jump in the light intensity after the locking resonator recorded as the mode-hopping monitoring signal (green curve in Figure 5-3(a)). It is seen that there were two mode-hopping events during the 1.5 s period of recording. The variations of two quasi-dc signals, I_{1d} and I_{2d}, shows that operating point changed during the data recording. The overall response of the system shows relatively uniform response to the simulated AE signal with a repetition rate of 100 Hz. Figure 5-3(b) is the enlarged view of the signal around the time when

the first mode-hopping occurred at around 2 seconds marked by a sharp increase in the intensity of the mode-hopping monitoring signal. A closer examination reveals that the mode-hopping event was also accompanied by step changes in the two quasi-DC components. It also shows that, preceding the mode-hopping, a simulated AE signal generated by the piezo actuator arrived at the sensor and was detected. A close-up view of the system signals at the time of the mode-hopping are shown in Figure 5-3(c). The two ac components signal, I_{1c} and I_{2c}, and the overall system output, I, show transient responses to the mode-hopping. The waveform shows an oscillation that only lasted less than two cycles and resembles the step response of a heavily damped bandpass filter. The pattern of the transient responses is different from the responses to the simulated AE signal, which is shown in Figure 5-3(d). The response to the AE signal shows a main wave packet with many cycles typical to AE signals. Therefore, we can conclude that the signals shown in Figure 5-3(c) were caused by the mode-hopping of the self-injection locked DFB diode laser but not by the AE signal. The system response to the second mode-hopping has the similar characteristics to those for the first mode-hopping. As shown in Figure 5-3(e), a step change in the mode-hopping signal indicates the occurrence of the second mode-hopping event and a simulated AE pulse arrived at the sensor about 1.5 ms after the mode-hopping event and was detected by the sensor. Note that, the mode-hopping signal shows a larger step change compared to the first mode-hopping. The change in the step size is related to the wavelength position of the locking point relative to the spectrum of FBG-FPI in the feedback loop (see Figure 5-4(a)) below. Figure 5-3(f) is the detailed views of the transient response due to the mode-hopping and the transient lasted about 120 μs. The mode-hopping did not affect the detection of the simulated AE signal as shown in Figure 5-3(g). We note that, transient response to mode-hopping last around 100 μs, which is likely determined by the detection bandwidth of the sensor system.

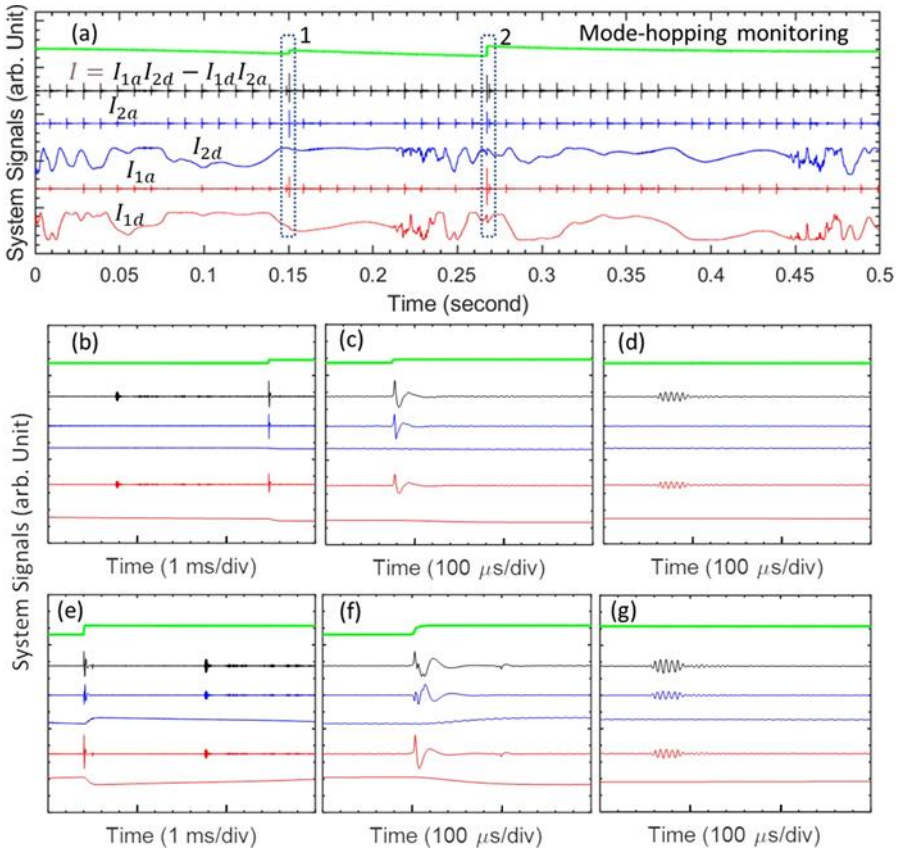

Figure 5.3 (a) Four-channel response with mode-hopping signal and overall ultrasonic response of the AE sensor system. (b) Enlarged view of Fig. 9(a) around the first mode-hopping event showing both the signal due to mode-hopping with more details shown in (c) and the response to the simulated AE signal with more details shown in (d); (e) Enlarged view of Fig. 9(a) around the second mode-hopping event showing both the signal due to the mode-hopping with more details shown in (f) and the response to the simulated AE signal with more details shown in (g).

In addition, a mode-hopping event can be reliably identified. Therefore, the transient signals due to the mode-hopping events can be reliably identified and removed from the overall signal. Note that according to the results shown in previous chapter, the laser could experience unstable operations that can accompany the mode-hopping events or occur spontaneously. Because they have distinct frequencies above the frequency range of the AE signal, they do not affect the operation of the sensor system.

5.4. Occurrence Frequencies of Mode-Hopping

As mentioned earlier, mode-hopping does not occur frequently for the self-injection locked DFB diode laser under laboratory environment. The laser can maintain stable operation over periods ranging from a few seconds to a few minutes. The experiment in section 5.3 were performed when external perturbation was intentionally introduced to the fiber feedback loop to induce more frequent mode-hopping of the locked laser. Here, we studied the mode-hopping events in the laboratory environment with no intentional perturbations. We paid attention to the occurrence frequency of mode-hopping events and the level of the intensity jump in the mode-hopping monitoring signal from the mode-hopping events in relation to the length of the self-injection locked feedback loop. As shown in Figure 5-4(a), the laser was locked to one of the external cavity modes close to the resonant peak of the FBG-FPI. The interval of the external cavity modes is determined by the free-spectral range (FSR) of external cavity (feedback loop) given by FSR $= \lambda^2/2nL$, where λ is the wavelength of operation, n is the refractive index of the fiber, and L is the length of the feedback loop. As schematically shown in Figure 5-4(a), shorter loop length provides a larger FSR and on average, a larger change in the optical loss between neighboring external modes, resulting in less frequent mode-hopping jump with on average, larger mode-hopping jump height because of the large distance between the external cavity modes. On the other hand, longer loop provides smaller FSR with denser sinusoidal fringes resulting in more frequent mode-hopping occurs with smaller jump levels due to the smaller distance between the external cavity modes, as schematically shown in Figure 5-4(b). We varied the fiber length of the feedback loop from 7 m to 24 m by including the fiber patch cables of various lengths in the feedback loop. For each loop length, we monitored the naturally occurring mode-hopping events of self-injection locked DFB laser by recording the mode-hopping monitoring signals for 1 hour.

Figure 5-4(c-g) show the results for loop lengths about 7 m, 9 m, 11 m, 14 m, and 24 m, respectively. The enlarged view of mode-hopping jumps for different loop lengths are also shown in the in-sets of Figure 5-4(c-g) as marked by a box and an arrow.

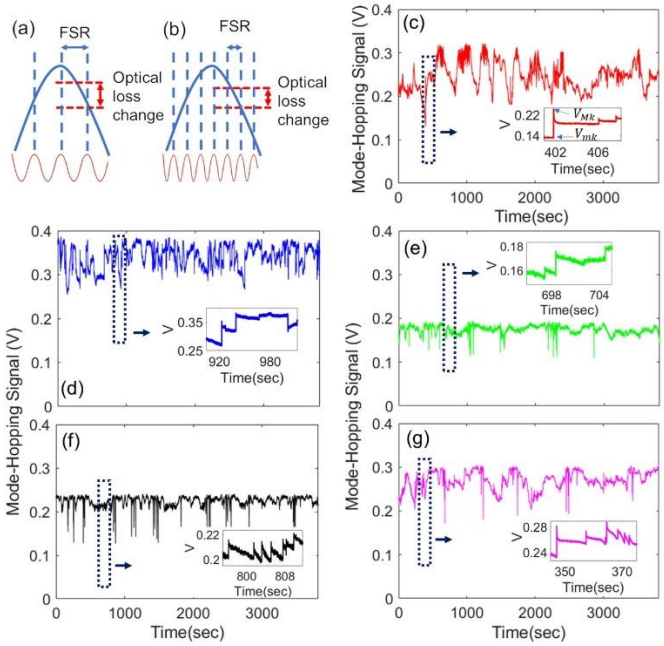

Figure 5.4 Schematic illustration of (a) shorter loop length with large FSR provides less frequent mode-hopping with larger change in optical loss (b) longer loop length with small FSR provides more frequent mode-hopping with smaller change in optical loss. Mode-hopping jumps of self-injection locked laser for fiber ring loop length of (c) 7 m, (d) 9 m, (e) 11 m, (f) 14 m, (g) 24 m. Insets: Enlarged view of mode-hopping for different loop lengths as marked by a box and an arrow.

In addition, we studied the effect of feedback loop length on mode-hopping occurrence frequency by counting the number of the jumps in the mode-hopping events. We have also estimated the average normalized height of mode-hopping jumps, $\bar{S}$, for different loop lengths of the self-injection locked DFB diode laser according to the following definition:

$$\bar{S}=\frac{1}{N}\sum_{k=1}^{N}\frac{V_{Mk}-V_{mk}}{(V_{Mk}+V_{mk})/2}, \tag{5.3}$$

N is the number of mode-hopping jumps during the period of monitoring, and V_{mk} and V_{Mk} are respectively, the signal level right before and after the jumping, as schematically shown in the inset of Figure 5-4(c).

Figure 5-5 shows the number of the recorded mode-hopping events and the average normalized height of mode-hopping jumps for different loop lengths, as well as the linear fittings of the data points. It demonstrates that, the number of mode-hopping increases with the increasing of loop-length. On the other hand, average normalized height of mode-hopping jump decreases with the increasing of loop length and number of mode-hopping. Both show a relatively good linear relationship with the feedback loop length. Therefore, number of mode-hopping is inversely proportional to the mode-hopping height.

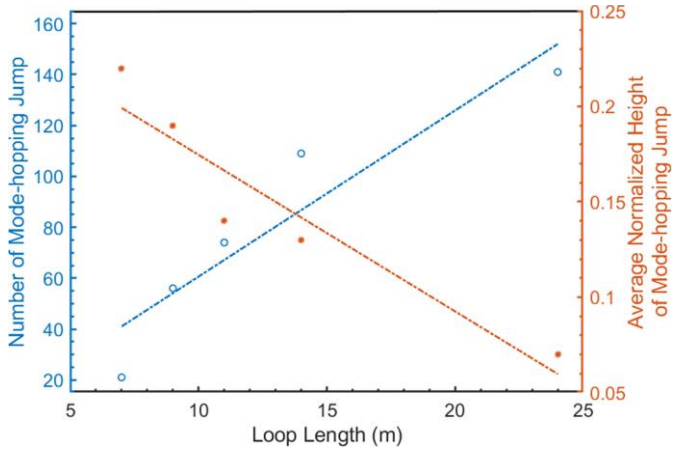

Figure 5.5 Relationship of loop length with number of mode-hopping and average normalized height of mode-hopping jump.

The results show that, in general, shorter loop lengths provided smaller number of mode-hopping events with larger jump heights. Therefore, reducing the feedback loop length can effectively reduce the number of mode-hopping events in a self-injection locked DFB diode laser. In the laboratory environment, 141 mode-hopping events were registered for self-injection locked

laser with the longest fiber loop length (24 m). On average, a mode-hopping event occurs every 25 seconds. As shown in Section III, the spurious transient signals from a mode-hopping event only lasted ~100 μs. Therefore, the disruption to the AE sensor system caused by removing the spurious signal from the mode-hopping event of the self-injection locked laser is likely insignificant and negligible.

It needs to be stressed that the experiment was performed in a laboratory environment. Larger perturbations that can be experienced in the field may cause more frequent mode- hopping and even unlocking of the laser if the discrepancy between the free-running laser wavelength and the resonator wavelength becomes large. As the minimum feedback loop length may still be on the order of meters due to the use of fiber-pigtailed lasers and other fiber-pigtailed components, the laser system is expected to be prone to environmental perturbations and likely needs to be packaged and protected for practical applications in the field. Active approaches, e.g., controlling the drift of the external cavity mode through a fiber stretcher, to minimize the mode-hopping could also be considered.

Chapter 6: Measurement of Absolute Strain Using Fiber-Optic Sensors

6.1. Research Objectives

In this project, we worked on the development of a "rf interferometer" with low order fringes so that the strain-induced rf spectral shift does not exceed half of the fringe period. It confirms the possibility of absolute strain measurement. Specifically, a sensor contains a span of fiber between two identical fiber-Bragg gratings (FBGs) and intensity-modulated laser light is injected into a fiber. The light reflected by the two identical FBGs on both ends of the fiber is detected and the signal contains two sinusoidal functions in the rf range with a phase delay related to the optical distance between the two FBGs. By scanning the modulation frequency, fringes in the rf range is obtained and the strain is obtained with high resolution and accuracy using the rf fringe shift.

6.2. Principle of Operation

The system is schematically shown in Figure 6-1. The sensing fiber contains an optical fiber between two identical FBGs. The wavelength of the FBGs for each sensor is unique. Assume the length of the fiber between the two FBGs of each sensor is L as shown in Figure 6-1. The intensity of a light source is modulated sinusoidally with a radian frequency of Ω. Note that Ω can be scanned over a range using a voltage-controlled oscillator (VCO). The modulated light is then sent to the fiber-optic sensor via an optical circulator. Each sensor reflects the light at a different wavelength. The reflected optical signals are then directed to an optical tunable filter to select the reflection from a sensor according to its wavelength. Because of the low coherence of the optical source and the relatively broad spectral width of the FBG reflection, the light reflected by the two FBGs of the sensor do not interfere and the output from the PD is proportional to the intensity summation of the two reflections, which travel different optical path lengths along the fiber before

it arrives at the PD. As the intensity of the light is modulated sinusoidally, this difference is reflected as a phase delay between the two modulated reflections.

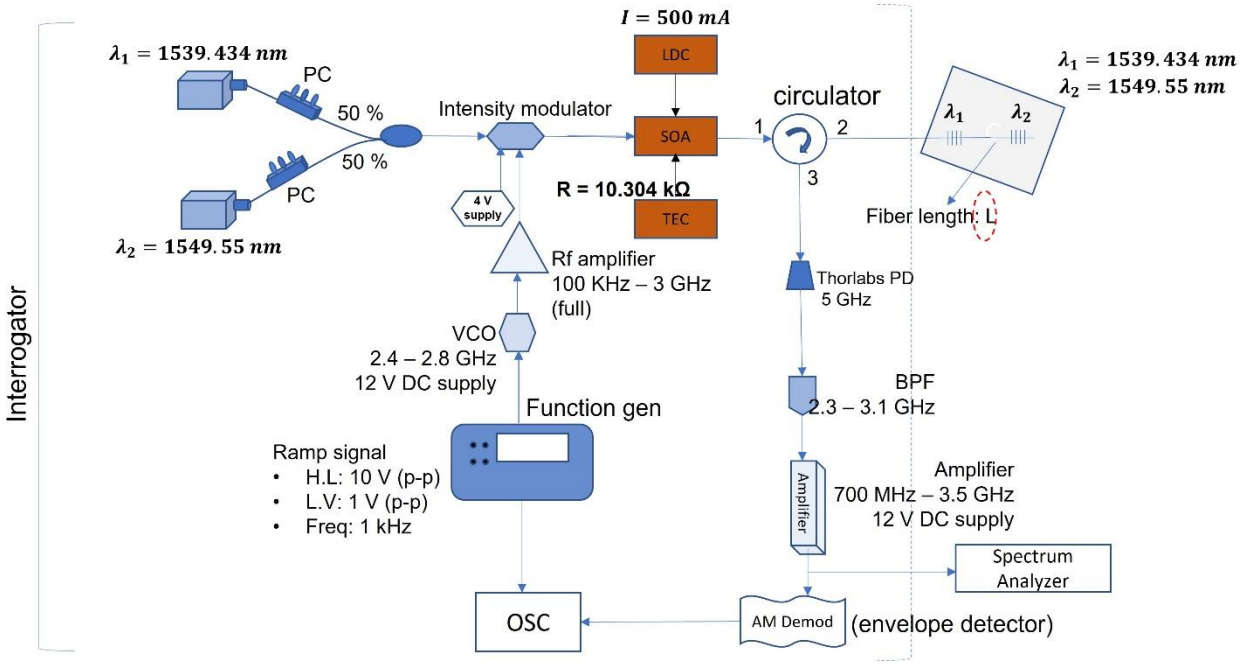

Figure 6.1 Schematic of the system. Int. Mod., intensity modulator; VCO, voltage-controlled oscillator; PD, photodetector.

For example, for the sensor with a fiber length of L between the two FBGs, the signal detected by the PD, $s(t)$, is given by 6.1

$$s_1(t)=D+A\cos(\Omega t+\varphi_0)+B\cos\left(\Omega t+\varphi_0+\frac{2\Omega nL}{c}\right) \tag{6.1}$$

where c is the speed of light in vacuum, D, A, and B are constants, and φ_0 is an arbitrary phase. In Eq. (6.1), we have assumed that the reflections from the two FBGs are identical. After passing through a band-pass filter to remove the dc component, the signal becomes

$$s_2(t)=A\cos(\Omega t+\varphi_0)+B\cos\left(\Omega t+\varphi_0+\frac{2\Omega nL}{c}\right) \tag{6.2}$$

which can be written as,

$$s_2(t)=\sqrt{A^2+B^2+2AB\cos\left(\frac{2\Omega nL}{c}\right)}\cos\left(\Omega t+\varphi_0+\Theta\right) \quad (6.3)$$

As the modulation frequency is scanned with a scanning frequency much smaller than Ω, Eq. (6.3) represents a AM-modulated signal and the modulation signal

$$s(t) \propto \sqrt{A^2+B^2+2AB\cos\left(\frac{2\Omega nL}{c}\right)} \quad (6.4)$$

can be obtained by an AM demodulator. As Ω is scanned over a range, we obtain $s(t)$ which is a periodical function of Ω. It can be considered as the "spectrum" of the "rf interferometer" formed by the two FBG reflectors of the sensor. The relative change of the optical distance, $\Delta(nL)/nL$, which is related to the strain of the structure when it is bonded on the surface, can be found from the spectral shift, Δf, as

$$\varepsilon=\frac{2\Delta(nL)}{nL}=2\Delta f/f \quad (6.5)$$

where $f = \Omega/2\pi$. Note that the factor of 2 in Eq. (6.3) accounts for the transfer from the linear strain of the structural surface to the relative change in the fiber length of the fiber bragg gratings.

Figure 6-2 shows demodulated sensor spectrum and Figure 6-3 shows the schematic diagram for absolute strain measurement. Output from the AM demodulator that can be shifted by strain applied to the fiber between two FBG sensors.

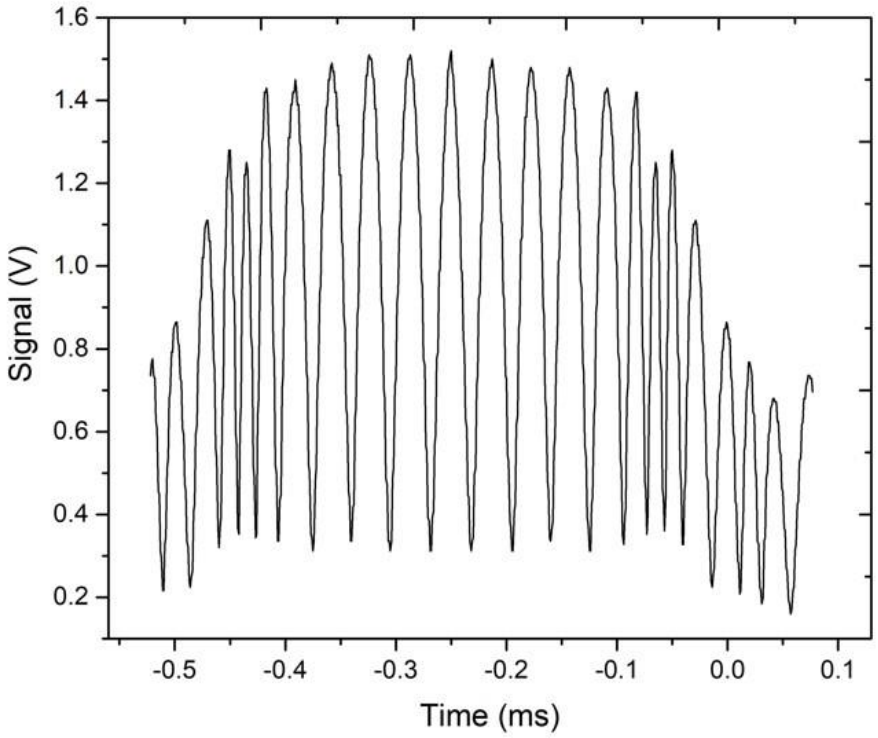

Figure 6.2 Demodulated sensor spectrum.

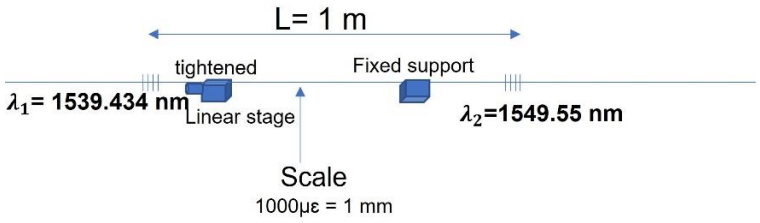

Figure 6.3 Schematic of strain measurement setup.

Figure 6-4 shows VCO tuning voltage as a scale on sensor spectrum to measure frequency which will be useful for strain measurement. Figure 6-5 shows stretched vs unstretched sensor spectrum where 5MHz frequency shift in the stretched fiber provides strain information as 2000 $\mu\varepsilon$ (as shown in Eq. (6.6)).

$$\varepsilon = \frac{\Delta(nL)}{nL} = \frac{\Delta f}{f} = \frac{5\ \text{MHz}}{2.4\ \text{GHz}} = 2000\ \mu\varepsilon \tag{6.6}$$

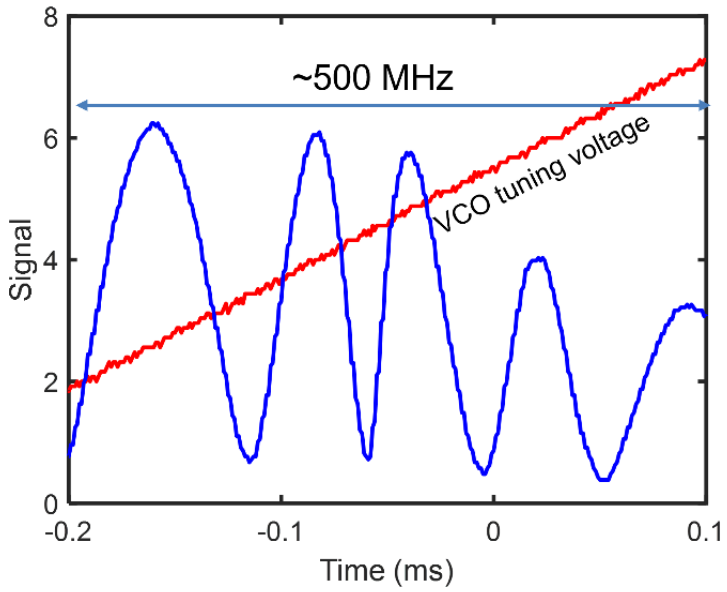

Figure 6.4 VCO tuning voltage as a scale to measure frequency change in sensor spectrum.

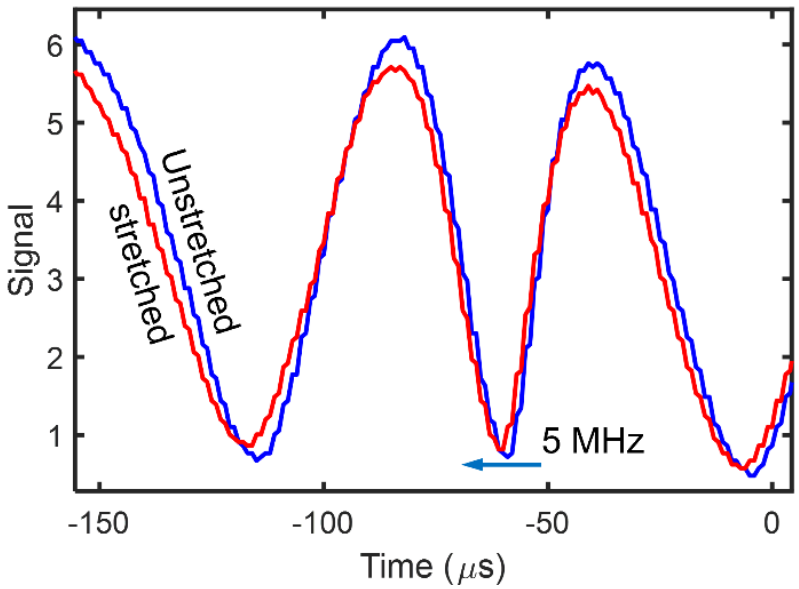

Figure 6.5 Stretched vs unstretched frequency shift to calculate strain on fiber optic sensor.

Figure 6-6 shows experimental setup to measure strain on fiber coil sensor where both FBGs are 20 cm apart. Figure 6-7 shows strain measurement technique on reference FBG sensor.

Reference FBG has peak at 1546 nm on reflection spectrum. Here, 1 με on reference FBG will contribute to 1 pm reference FBG spectral peak shift. In similar way, 1000 με on reference FBG will contribute to 1 nm reference FBG spectral peak shift.

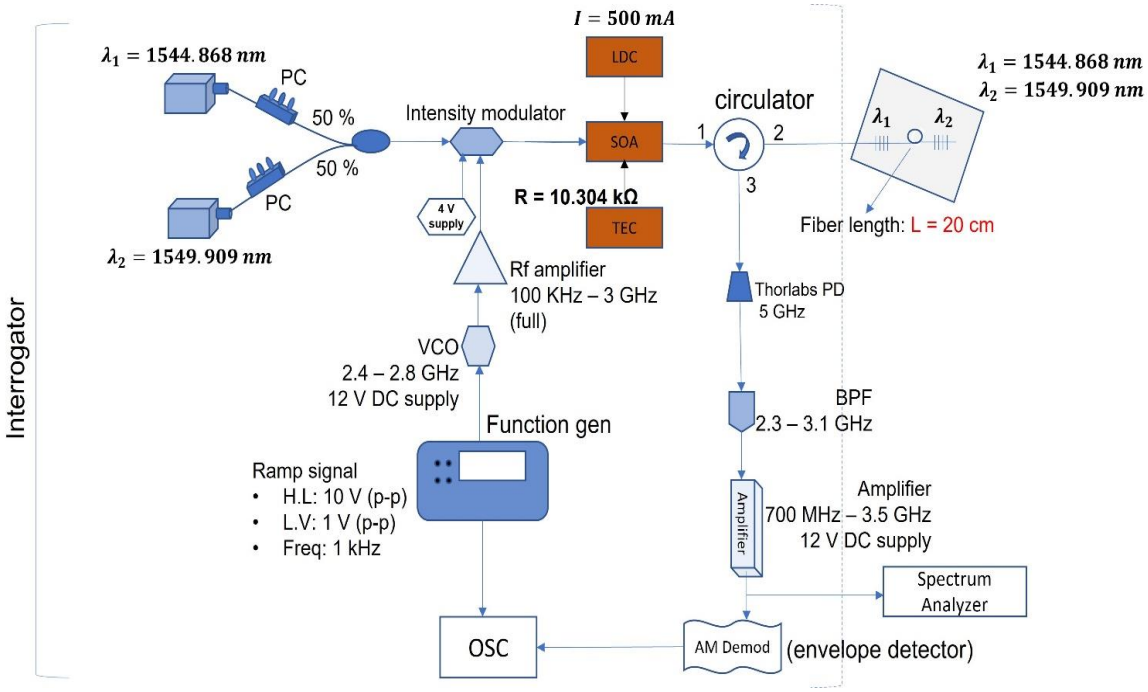

Figure 6.6 Experimental setup to measure strain using fiber coil sensor.

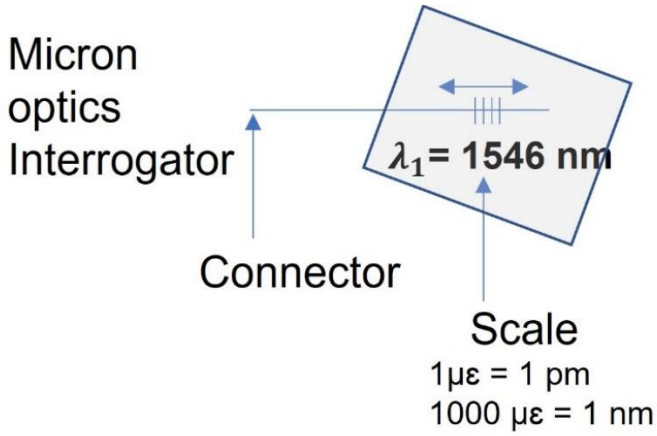

Figure 6.7 Reference FBG sensor to measure strain on fiber coil sensors.

Figure 6-8 shows the pictorial view for fiber coil strain measurement technique where fiber coil sensor is attached on Al plate in parallel with reference FBG to find it`s strain performance.

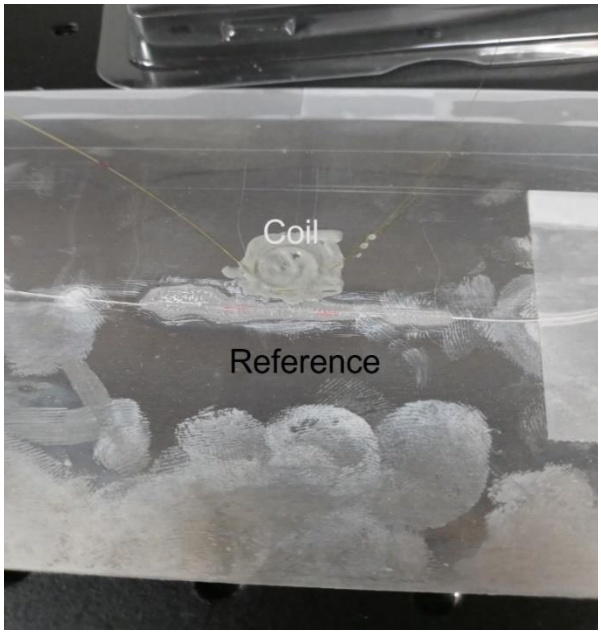

Figure 6.8 Attachment of fiber coil sensor on Al plate in parallel of reference FBG sensor for strain measurement.

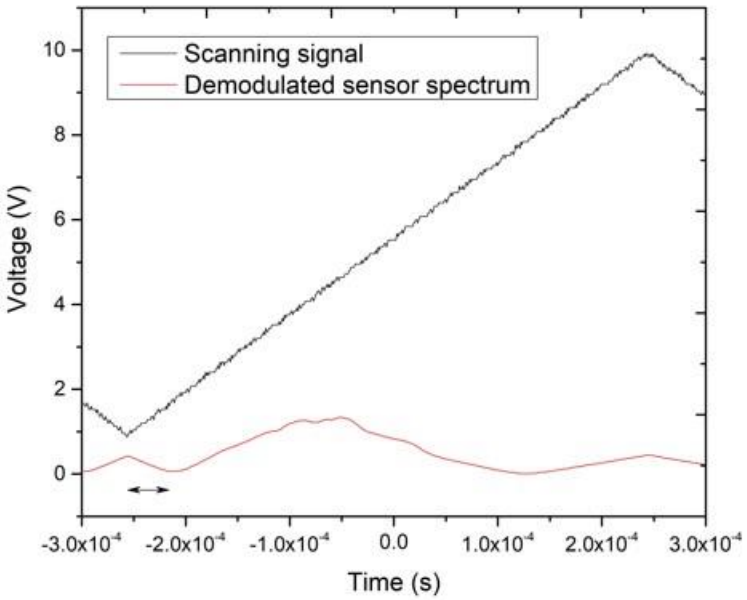

Figure 6.9 Demodulated fiber coil sensor spectrum valley point as indicated by arrow with respect to scanning signal valley.

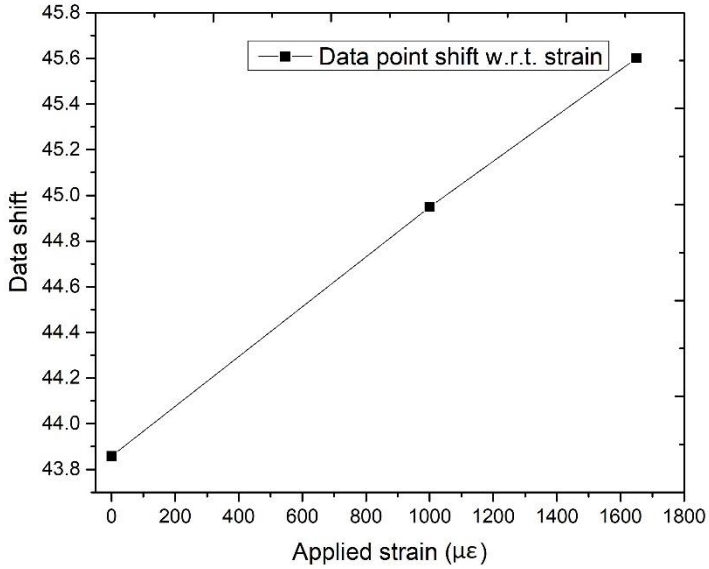

Figure 6.10 Data point shift with applied strain on fiber coil sensors.

Figure 6-9 shows demodulated fiber coil sensor spectrum. Fiber coil sensor spectrum valley point with respect to scanning signal valley point can help to measure the strain applied to sensor. Fiber coil sensor spectrum valley point will shift with respect to scanning signal valley point based on the strain applied. The applied strain on the fiber coil sensor can be calculated using Eq. (6.6).

Figure 6-10 shows the fiber coil sensor spectrum valley point shift with respect to scanning signal valley point with the applied strain.

6.3. Strain range without phase ambiguity:

The fringe order from this rf interference is much lower than that from an optical interference of the same length. For example, the period of the spectral fringes is 100 MHz for 1 m of optical fiber between the two FBGs and fringe order is about 10 when the center modulation frequency f = 1 GHz. In this case, a frequency shift of half fringe period corresponds to a strain

range of 10% (100,000 με), which typically exceeds the maximum strain that a structure can potentially have in practice.

6.4. Strain Measurement Resolution:

Assuming n is a constant, from Eq. (6.2), the measurement resolution of overall strain measurement can be estimated by

$$\Delta\varepsilon_{res}=2\Delta f_{res}/f \tag{6.7}$$

where Δf_{res} is the resolution in determining the frequency shift of the spectrum of the rf interferometer. Assuming a frequency resolution of 10 kHz from a VCO centered at 1 GHz, the strain measurement resolution is then $\Delta\varepsilon_{res} = 20$ με.

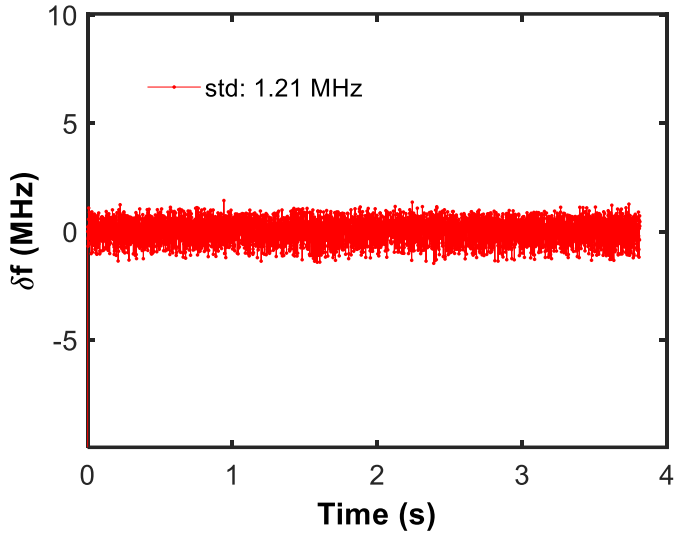

Figure 6.11 Strain measurement resolution on fiber coil sensor when FBGs are 20 cm apart.

Figure 6-11 shows the strain measurement resolution on fiber coil sensor when both FBGs are 20 cm apart and diameter of the coil is 1 cm. Here, $\Delta\varepsilon_{res} = 500$ με.

Chapter 7: Summary and Future work

7.1. Summary

In summary, we have analyzed the steady-state solutions to the rate equation model that describes a DFB diode laser with coherent filtered optical feedback from a long fiber-optic loop. We found that the laser wavelength is mainly determined by the external cavity mode and can drift due to the phase delay changes. We propose to suppress the drift by actively controlling the phase delay. The error signal is obtained by modulating the filter wavelength and recording the transmitted signal of the filter. The results from the experiment to demonstrate the operating principle agrees with the theory in general. The wavelength drift was estimated to be reduced by ~75% compared with the case without phase delay control. The active control of phase delay does not cause noticeable broadening of the beat note within the limit of the measurement resolution.

We also studied the mode-hopping and laser instability as well as their effect on the performance of the sensor system. Experimental results demonstrate that, the mode-hopping of self-injection locked DFB laser induced transient responses that lasted only around 100 μs. The laser instable operation characterized by the laser frequency oscillations can accompany the mode-hopping or occur spontaneously without mode-hopping.

A self-injection locked DFB diode laser AE sensor system has been demonstrated using a fiber optic interferometric sensor through a modified PGC demodulation method. The self-injection locked DFB diode laser had a narrow notch filter of 1.5 pm linewidth which served as a locking resonator in a fiber ring feedback loop. We locked the laser wavelength to an external cavity mode on the spectral slope of the filter. The self-injection locked DFB diode laser ultrasonic sensor system proposed in this work provided ~33 dB higher SNR than that of a DFB diode laser in free-running mode. We also studied the mode-hopping and laser instability as well as their effect on

the performance of the sensor system. Experimental results demonstrate that, the mode-hopping of self-injection locked DFB laser induced transient responses that lasted only around 100 μs. The mode-hopping induced response can be identified and removed with negligible impact on the detection of the AE signal. The laser instable operation characterized by the laser frequency oscillations can accompany the mode-hopping or occur spontaneously without mode-hopping. We found that the oscillations have spectral components at discrete frequencies much higher than the AE frequency and do not affect the performance of the sensor performance. In addition, experimental results show that, we could also reduce the occurrence frequency of mode-hopping events by reducing the loop length and thus increasing the spectral spacing of the external cavity modes.

Finally, a novel technique is developed for the measurement of absolute strain using fiber-optic sensors.

7.2. Future work

We present a method to suppress the wavelength drift of a DFB laser with filtered coherent optical feedback through a relatively long fiber-optic loop by actively controlling the phase delay of the feedback light to align the external cavity mode with the transmission peak of the resonator in the loop. A limitation of the experiment is the low speed of the phase delay control system that includes a cantilever beam and motorized stage. Improvement over the feedback speed using, e.g., a piezoelectric fiber stretcher may provide better stabilization performance.

With the identification of the mode-hopping events, the associated spurious signal can be identified and discarded in the signal processing without causing significant disruption to the sensor system.

Fiber optic strain sensor data can be applied to deep learning or, machine learning algorithms for efficient SHM of civil structures as discussed in chapter 1.

REFERENCES

[1] H. Li and H. R. Telle, “Efficient frequency noise reduction of GaAlAs semiconductor lasers by optical feedback from an external high-finesse resonator,” *IEEE Journal of Quantum Electronics*, vol. 25, no. 3, pp. 257–264, 1989, doi: 10.1109/3.18538.

[2] P. Laurent, A. Clairon, and C. Breant, “Frequency noise analysis of optically self-locked diode lasers,” *IEEE Journal of Quantum Electronics*, vol. 25, no. 6, pp. 1131–1142, 1989, doi: 10.1109/3.29238.

[3] A. P. A. Fischer, M. Yousefi, D. Lenstra, M. W. Carter, and G. Vemuri, “Filtered Optical Feedback Induced Frequency Dynamics in Semiconductor Lasers,” *Phys. Rev. Lett.*, vol. 92, no. 2, p. 023901, Jan. 2004, doi: 10.1103/PhysRevLett.92.023901.

[4] W. Lewoczko-Adamczyk *et al.*, “Ultra-narrow linewidth DFB-laser with optical feedback from a monolithic confocal Fabry-Perot cavity,” *Opt. Express*, vol. 23, no. 8, pp. 9705–9709, Apr. 2015, doi: 10.1364/OE.23.009705.

[5] W. Liang *et al.*, “Ultralow noise miniature external cavity semiconductor laser,” *Nature Communications*, vol. 6, no. 1, p. 7371, Jun. 2015, doi: 10.1038/ncomms8371.

[6] J. L. B. Escobedo *et al.*, “Distributed measurements of vibration frequency using phase-OTDR with a DFB laser self-stabilized through PM fiber ring cavity,” *Results in Physics*, vol. 12, pp. 1840–1842, 2019, doi: https://doi.org/10.1016/j.rinp.2019.02.023.

[7] X. Zhu, X. Li, R. Zhang, Z. Zhao, and M. Kong, “Using DFB laser self-injection locked to an optical waveguide ring resonator as a light source of Φ-OTDR,” *Appl. Opt.*, vol. 60, no. 31, pp. 9769–9773, Nov. 2021, doi: 10.1364/AO.438572.

[8] J. Geng, L. Yang, S. Zhao, and Y. Zhang, “Resonant micro-optical gyro based on self-injection locking,” *Opt. Express*, vol. 28, no. 22, pp. 32907–32915, Oct. 2020, doi: 10.1364/OE.405974.

[9] A. D. Kersey *et al.*, “Fiber grating sensors,” *Journal of Lightwave Technology*, vol. 15, no. 8, pp. 1442–1463, 1997, doi: 10.1109/50.618377.

[10] S. O’Keeffe, D. McCarthy, P. Woulfe, J. Cronin, and E. Lewis, “Optical Fibre Based Scintillation Probe for Radiotherapy Dosimetry,” in *Imaging and Applied Optics Technical Papers*, Optica Publishing Group, 2012, p. AM3A.3. doi: 10.1364/AIO.2012.AM3A.3.

[11] M. Anwar Zawawi, S. O’Keffe, and E. Lewis, “Intensity-modulated fiber optic sensor for health monitoring applications: a comparative review,” *Sensor Review*, vol. 33, no. 1, pp. 57–67, Jan. 2013, doi: 10.1108/02602281311294351.

[12] Y. Zhu and A. Wang, “Miniature fiber-optic pressure sensor,” *IEEE Photonics Technology Letters*, vol. 17, no. 2, pp. 447–449, 2005, doi: 10.1109/LPT.2004.839002.

[13] Y.-J. Rao, D. J. Webb, D. A. Jackson, L. Zhang, and I. Bennion, “In-fiber Bragg-grating temperature sensor system for medical applications,” *Journal of Lightwave Technology*, vol. 15, no. 5, pp. 779–785, 1997, doi: 10.1109/50.580812.

[14] N. Sabri, S. A. Aljunid, M. S. Salim, and S. Fouad, “Fiber Optic Sensors: Short Review and Applications,” in *Recent Trends in Physics of Material Science and Technology*, F. L. Gaol, K. Shrivastava, and J. Akhtar, Eds., Singapore: Springer Singapore, 2015, pp. 299–311. doi: 10.1007/978-981-287-128-2_19.

[15] P. Navratil *et al.*, “Self-swept erbium fiber laser around 1.56 μm,” *Opto-Electronics Review*, vol. 26, no. 1, pp. 29–34, 2018, doi: https://doi.org/10.1016/j.opelre.2017.11.004.

[16] M. Michalska, W. Brojek, Z. Rybak, P. Sznelewski, M. Mamajek, and J. Swiderski, “Highly stable, efficient Tm-doped fiber laser—a potential scalpel for low invasive surgery,” *Laser Physics Letters*, vol. 13, no. 11, p. 115101, Sep. 2016, doi: 10.1088/1612-2011/13/11/115101.

[17] P. Peterka, P. Honzátko, I. Ka\vsík, J. Cajzl, and O. Podrazký, “Thulium-doped optical fibers and components for fiber lasers in 2 μm spectral range,” in *Wave and Quantum Aspects of Contemporary Optics*, 2014.

[18] C. B. Scruby, “An introduction to acoustic emission,” *Journal of Physics E: Scientific Instruments*, vol. 20, no. 8, p. 946, Aug. 1987, doi: 10.1088/0022-3735/20/8/001.

[19] D. C. Betz, G. Thursby, B. Culshaw, and W. J. Staszewski, “Acousto-ultrasonic sensing using fiber Bragg gratings,” *Smart Materials and Structures*, vol. 12, no. 1, p. 122, Jan. 2003, doi: 10.1088/0964-1726/12/1/314.

[20] Q. Wu, Y. Okabe, and F. Yu, “Ultrasonic Structural Health Monitoring Using Fiber Bragg Grating,” *Sensors*, vol. 18, no. 10, 2018, doi: 10.3390/s18103395.

[21] M. Majumder, T. K. Gangopadhyay, A. K. Chakraborty, K. Dasgupta, and D. K. Bhattacharya, “Fibre Bragg gratings in structural health monitoring—Present status and applications,” *Sensors and Actuators A: Physical*, vol. 147, no. 1, pp. 150–164, 2008, doi: https://doi.org/10.1016/j.sna.2008.04.008.

[22] Q. Zhang, Y. Zhu, X. Luo, G. Liu, and M. Han, “Acoustic emission sensor system using a chirped fiber-Bragg-grating Fabry–Perot interferometer and smart feedback control,” *Opt. Lett.*, vol. 42, no. 3, pp. 631–634, Feb. 2017, doi: 10.1364/OL.42.000631.

[23] G. Liu and M. Han, “Wavelength Locking of a Diode Laser to the Maximal Slope of a π -Phase-Shifted Fiber Bragg Grating for Acoustic Emission Detection,” *IEEE Sensors Journal*, vol. 18, no. 22, pp. 9257–9262, 2018, doi: 10.1109/JSEN.2018.2869799.

[24] T. Liu and M. Han, “Analysis of π -Phase-Shifted Fiber Bragg Gratings for Ultrasonic Detection,” *IEEE Sensors Journal*, vol. 12, no. 7, pp. 2368–2373, 2012, doi: 10.1109/JSEN.2012.2189383.

[25] S. Taccheo *et al.*, “Challenges and future trends in fiber lasers,” *2016 18th International Conference on Transparent Optical Networks (ICTON)*, pp. 1–5, 2016.

[26] J. Sotor *et al.*, “All-fiber Ho-doped mode-locked oscillator based on a graphene saturable absorber,” *Opt. Lett.*, vol. 41, no. 11, pp. 2592–2595, Jun. 2016, doi: 10.1364/OL.41.002592.

[27] N. M. Kondratiev *et al.*, “Self-injection locking of a laser diode to a high-Q WGM microresonator,” *Opt. Express*, vol. 25, no. 23, pp. 28167–28178, Nov. 2017, doi: 10.1364/OE.25.028167.

[28] R. W. P. Drever *et al.*, “Laser phase and frequency stabilization using an optical resonator,” *Applied Physics B*, vol. 31, no. 2, pp. 97–105, Jun. 1983, doi: 10.1007/BF00702605.

[29] A. D. Ludlow *et al.*, “Compact, thermal-noise-limited optical cavity for diode laser stabilization at 1×10\textminus15,” *Opt. Lett.*, vol. 32, no. 6, pp. 641–643, Mar. 2007, doi: 10.1364/OL.32.000641.

[30] J. Alnis, A. Matveev, N. Kolachevsky, Th. Udem, and T. W. Hänsch, “Subhertz linewidth diode lasers by stabilization to vibrationally and thermally compensated ultralow-expansion glass Fabry-Pérot cavities,” *Phys. Rev. A*, vol. 77, no. 5, p. 053809, May 2008, doi: 10.1103/PhysRevA.77.053809.

[31] M. Kourogi and M. Ohtsu, “Novel optical frequency discriminator for FM noise reduction of semiconductor lasers,” *Optics Communications*, vol. 81, no. 3, pp. 204–208, 1991, doi: https://doi.org/10.1016/0030-4018(91)90639-U.

[32] W. Liang, V. S. Ilchenko, A. A. Savchenkov, A. B. Matsko, D. Seidel, and L. Maleki, “Whispering-gallery-mode-resonator-based ultranarrow linewidth external-cavity semiconductor laser,” *Opt. Lett.*, vol. 35, no. 16, pp. 2822–2824, Aug. 2010, doi: 10.1364/OL.35.002822.

[33] V. V. Vassiliev, V. L. Velichansky, V. S. Ilchenko, M. L. Gorodetsky, L. Hollberg, and A. V. Yarovitsky, “Narrow-line-width diode laser with a high-Q microsphere resonator,” *Optics Communications*, vol. 158, no. 1, pp. 305–312, 1998, doi: https://doi.org/10.1016/S0030-4018(98)00578-1.

[34] V. V. Vassiliev, S. M. Il’ina, and V. L. Velichansky, “Diode laser coupled to a high-Q microcavity via a GRIN lens,” *Applied Physics B*, vol. 76, no. 5, pp. 521–523, May 2003, doi: 10.1007/s00340-003-1151-5.

[35] C. A. López-Mercado *et al.*, “Locking of the DFB laser through fiber optic resonator on different coupling regimes,” *Optics Communications*, vol. 359, pp. 195–199, 2016, doi: https://doi.org/10.1016/j.optcom.2015.09.076.

[36] J. L. B. Escobedo, V. V. Spirin, C. A. López-Mercado, P. Mégret, I. O. Zolotovskii, and A. A. Fotiadi, “Self-injection locking of the DFB laser through an external ring fiber cavity:

Polarization behavior," *Results in Physics*, vol. 6, pp. 59–60, 2016, doi: https://doi.org/10.1016/j.rinp.2016.01.017.

[37] D. A. Korobko, I. O. Zolotovskii, K. Panajotov, V. V. Spirin, and A. A. Fotiadi, "Self-injection-locking linewidth narrowing in a semiconductor laser coupled to an external fiber-optic ring resonator," *Optics Communications*, vol. 405, pp. 253–258, 2017, doi: https://doi.org/10.1016/j.optcom.2017.08.040.

[38] C. Wang, R. Zhang, Z. Zhao, C. Chen, and M. Kong, "Comparison of Self-Injection Locking of DFB-LD by Optical Fiber and Optical Waveguide Ring Resonators," *Fiber and Integrated Optics*, vol. 38, no. 6, pp. 323–332, 2019, doi: 10.1080/01468030.2019.1704098.

[39] A. V. Kir'yanov and N. N. Il'ichev, "Self-induced laser line sweeping in an ytterbium fiber laser with non-resonant Fabry-Perot cavity," *Laser Physics Letters*, vol. 8, no. 4, p. 305, Jan. 2011, doi: 10.1002/lapl.201010138.

[40] P. Peterka *et al.*, "Reflectivity of transient Bragg reflection gratings in fiber laser with laser-wavelength self-sweeping," *Opt. Express*, vol. 22, no. 24, pp. 30024–30031, Dec. 2014, doi: 10.1364/OE.22.030024.

[41] F. Wei *et al.*, "Subkilohertz linewidth reduction of a DFB diode laser using self-injection locking with a fiber Bragg grating Fabry-Perot cavity.," *Opt Express*, vol. 24, no. 15, pp. 17406–17415, Jul. 2016, doi: 10.1364/OE.24.017406.

[42] V. V. Spirin, J. L. B. Escobedo, D. A. Korobko, P. Mégret, and A. A. Fotiadi, "Stabilizing DFB laser injection-locked to an external fiber-optic ring resonator," *Opt. Express*, vol. 28, no. 1, pp. 478–484, Jan. 2020, doi: 10.1364/OE.28.000478.

[43] L. Hao *et al.*, "Narrow-linewidth self-injection locked diode laser with a high-Q fiber Fabry–Perot resonator," *Opt. Lett.*, vol. 46, no. 6, pp. 1397–1400, Mar. 2021, doi: 10.1364/OL.415859.

[44] R. Abbasnia and A. Farsaei, "Corrosion detection of reinforced concrete beams with wavelet analysis," *International Journal of Civil Engineering*, vol. 11, no. 3. pp. 160–169, 2013.

[45] F. Surre, T. Sun, and K. T. Grattan, "Fiber Optic Strain Monitoring for Long-Term Evaluation of a Concrete Footbridge Under Extended Test Conditionss," *IEEE Sensors Journal*, vol. 13, no. 3, pp. 1036–1043, 2013, doi: 10.1109/JSEN.2012.2234736.

[46] U. M. N. Jayawickrema, H. M. C. M. Herath, N. K. Hettiarachchi, H. P. Sooriyaarachchi, and J. A. Epaarachchi, "Fibre-optic sensor and deep learning-based structural health monitoring systems for civil structures: A review," *Measurement*, vol. 199, p. 111543, 2022, doi: https://doi.org/10.1016/j.measurement.2022.111543.

[47] K. Bednarska *et al.*, "Hybrid Fiber Optic Sensor Systems in Structural Health Monitoring in Aircraft Structures," *Materials*, vol. 13, no. 10, 2020, doi: 10.3390/ma13102249.

[48] R. Di Sante, "Fibre Optic Sensors for Structural Health Monitoring of Aircraft Composite Structures: Recent Advances and Applications," *Sensors*, vol. 15, no. 8, pp. 18666–18713, 2015, doi: 10.3390/s150818666.

[49] H. Murayama, D. Wada, and H. Igawa, "Structural health monitoring by using fiber-optic distributed strain sensors with high spatial resolution," *Photonic Sensors*, vol. 3, no. 4, pp. 355–376, Dec. 2013, doi: 10.1007/s13320-013-0140-5.

[50] S. Kavitha, R. J. Daniel, and K. Sumangala, "A simple analytical design approach based on computer aided analysis of bulk micromachined piezoresistive MEMS accelerometer for concrete SHM applications," *Measurement*, vol. 46, no. 9, pp. 3372–3388, 2013, doi: https://doi.org/10.1016/j.measurement.2013.05.013.

[51] S. Kavitha, R. J. Daniel, and K. Sumangala, "High performance MEMS accelerometers for concrete SHM applications and comparison with COTS accelerometers," *Mechanical Systems and Signal Processing*, vol. 66–67, pp. 410–424, 2016, doi: https://doi.org/10.1016/j.ymssp.2015.06.005.

[52] A. Ali, T. Y. Sandhu, and M. Usman, "Ambient Vibration Testing of a Pedestrian Bridge Using Low-Cost Accelerometers for SHM Applications," *Smart Cities*, vol. 2, no. 1, pp. 20–30, 2019, doi: 10.3390/smartcities2010002.

[53] S. Kavitha, R. J. Daniel, and K. Sumangala, "Design and Analysis of MEMS Comb Drive Capacitive Accelerometer for SHM and Seismic Applications," *Measurement*, vol. 93, pp. 327–339, 2016, doi: https://doi.org/10.1016/j.measurement.2016.07.029.

[54] S. Li and X. Peng, "Safety monitoring of underground steel pipeline subjected to soil deformation using wireless inclinometers," *Journal of Civil Structural Health Monitoring*, vol. 6, no. 4, pp. 739–749, Sep. 2016, doi: 10.1007/s13349-016-0194-3.

[55] D. W. Ha, H. S. Park, S. W. Choi, and Y. Kim, "A Wireless MEMS-Based Inclinometer Sensor Node for Structural Health Monitoring," *Sensors*, vol. 13, no. 12, pp. 16090–16104, 2013, doi: 10.3390/s131216090.

[56] S. Hou, C. Zeng, H. Zhang, and J. Ou, "Monitoring interstory drift in buildings under seismic loading using MEMS inclinometers," *Construction and Building Materials*, vol. 185, pp. 453–467, 2018, doi: https://doi.org/10.1016/j.conbuildmat.2018.07.087.

[57] S. Li, C. Wei, and X. Peng, "Safety Monitoring of Buried Pipeline with Socket Joints Subjected to Ground Deformation Using MEMS Inclinometers," *Journal of Pipeline Systems Engineering and Practice*, vol. 10, no. 2, p. 04019008, 2019, doi: 10.1061/(ASCE)PS.1949-1204.0000380.

[58] W. Zhang, L. M. Sun, and S. W. Sun, “Bridge-Deflection Estimation through Inclinometer Data Considering Structural Damages,” *Journal of Bridge Engineering*, vol. 22, no. 2, p. 04016117, 2017, doi: 10.1061/(ASCE)BE.1943-5592.0000979.

[59] K. Y. Koo, J. M. W. Brownjohn, D. I. List, and R. Cole, “Structural health monitoring of the Tamar suspension bridge,” *Structural Control and Health Monitoring*, vol. 20, no. 4, pp. 609–625, 2013, doi: https://doi.org/10.1002/stc.1481.

[60] T. Miyashita and M. Nagai, “Vibration-based structural health monitoring for bridges using laser doppler vibrometers and MEMS-based technologies,” *Int. J. Steel Struct.*, vol. 8, no. 12. pp. 325–331, 2008.

[61] J. Kwiatkowski, W. Anigacz, and D. Beben, “Comparison of Non-Destructive Techniques for Technological Bridge Deflection Testing,” *Materials*, vol. 13, no. 8, 2020, doi: 10.3390/ma13081908.

[62] N. de Battista, R. Westgate, K. Y. Koo, and J. Brownjohn, “Wireless monitoring of the longitudinal displacement of the Tamar Suspension Bridge deck under changing environmental conditions,” in *Sensors and Smart Structures Technologies for Civil, Mechanical, and Aerospace Systems 2011*, M. Tomizuka, Ed., SPIE, 2011, p. 79811O. doi: 10.1117/12.879811.

[63] Sie\’nko, Rafal, Bednarski, Lukasz, and Howiacki, Tomasz, “Continuous structural health monitoring of selected geotechnical quantities within Ko\’sciuszko Mound in Cracow,” *MATEC Web Conf.*, vol. 117, p. 00157, 2017, doi: 10.1051/matecconf/201711700157.

[64] C. Gentile, A. Ruccolo, and F. Canali, “Continuous monitoring of the Milan Cathedral: dynamic characteristics and vibration-based SHM,” *Journal of Civil Structural Health Monitoring*, vol. 9, no. 5, pp. 671–688, Nov. 2019, doi: 10.1007/s13349-019-00361-8.

[65] F. J. Carrión, J. A. Quintana, and S. E. Crespo, “SHM of a stayed bridge during a structural failure, case study: the Rio Papaloapan Bridge,” *Journal of Civil Structural Health Monitoring*, vol. 7, no. 2, pp. 139–151, Apr. 2017, doi: 10.1007/s13349-017-0221-z.

[66] T. Wandowski *et al.*, “Embedded Damage Localization Subsystem Based on Elastic Wave Propagation,” *Computer-Aided Civil and Infrastructure Engineering*, vol. 30, no. 8, pp. 654–665, 2015, doi: https://doi.org/10.1111/mice.12129.

[67] Y. Hu and Y. Yang, “Wave propagation modeling of the PZT sensing region for structural health monitoring,” *Smart Materials and Structures*, vol. 16, no. 3, p. 706, Apr. 2007, doi: 10.1088/0964-1726/16/3/018.

[68] F. Li, H. Li, J. Qiu, and G. Meng, “Guided wave propagation in H-beam and probability-based damage localization,” *Structural Control and Health Monitoring*, vol. 24, no. 5, p. e1916, 2017, doi: https://doi.org/10.1002/stc.1916.

[69] C.-P. Fritzen, R. T. Schulte, and H. Jung, “A modelling approach for virtual development of wave based SHM systems,” *Journal of Physics: Conference Series*, vol. 305, no. 1, p. 012071, Jul. 2011, doi: 10.1088/1742-6596/305/1/012071.

[70] M. Gresil, A. Poohsai, and N. Chandarana, “Guided Wave Propagation and Damage Detection in Composite Pipes Using Piezoelectric Sensors,” *Procedia Engineering*, vol. 188. pp. 148–155, 2017. doi: 10.1016/j.proeng.2017.04.468.

[71] C. Grosse, G. McLaskey, S. Bachmaier, S. D. Glaser, and M. Krüger, “A hybrid wireless sensor network for acoustic emission testing in SHM,” in *Sensors and Smart Structures Technologies for Civil, Mechanical, and Aerospace Systems 2008*, M. Tomizuka, Ed., SPIE, 2008, p. 693238. doi: 10.1117/12.775641.

[72] S. C. Lovejoy, “Acoustic Emission Testing of Beams to Simulate SHM of Vintage Reinforced Concrete Deck Girder Highway Bridges,” *Structural Health Monitoring*, vol. 7, no. 4, pp. 329–346, 2008, doi: 10.1177/1475921708090567.

[73] M. A. A. Aldahdooh and N. Muhamad Bunnori, “Crack classification in reinforced concrete beams with varying thicknesses by mean of acoustic emission signal features,” *Construction and Building Materials*, vol. 45. pp. 282–288, 2013. doi: 10.1016/j.conbuildmat.2013.03.090.

[74] P. Mirgal, J. Pal, and S. Banerjee, “Online acoustic emission source localization in concrete structures using iterative and evolutionary algorithms,” *Ultrasonics*, vol. 108. 2020. doi: 10.1016/j.ultras.2020.106211.

[75] A. Güemes, A. Fernández-López, P. F. Díaz-Maroto, A. Lozano, and J. Sierra-Perez, “Structural Health Monitoring in Composite Structures by Fiber-Optic Sensors,” *Sensors*, vol. 18, no. 4, 2018, doi: 10.3390/s18041094.

[76] N. D. W. Glossop *et al.*, “Optical fibre damage detection for an aircraft composite leading edge,” *Composites*, vol. 21, no. 1, pp. 71–80, 1990, doi: https://doi.org/10.1016/0010-4361(90)90100-B.

[77] J. Huang *et al.*, “Polymer optical fiber for large strain measurement based on multimode interference,” *Opt. Lett.*, vol. 37, no. 20, pp. 4308–4310, Oct. 2012, doi: 10.1364/OL.37.004308.

[78] R.-T. Wu and M. R. Jahanshahi, “Data fusion approaches for structural health monitoring and system identification: Past, present, and future,” *Structural Health Monitoring*, vol. 19, no. 2, pp. 552–586, 2020, doi: 10.1177/1475921718798769.

[79] F. Favre and D. Guen, “Spectral properties of a semiconductor laser coupled to a single mode fiber resonator,” *IEEE Journal of Quantum Electronics*, vol. 21, no. 12, pp. 1937–1946, 1985, doi: 10.1109/JQE.1985.1072600.

[80] R. Lang and K. Kobayashi, “External optical feedback effects on semiconductor injection laser properties,” *IEEE Journal of Quantum Electronics*, vol. 16, no. 3, pp. 347–355, 1980, doi: 10.1109/JQE.1980.1070479.

[81] M. Yousefi, D. Lenstra, G. Vemuri, and A. Fischer, “Control of nonlinear dynamics of a semiconductor laser with filtered optical feedback,” *IEE Proceedings - Optoelectronics*, vol. 148, no. 5, pp. 233-237(4), Dec. 2001.

[82] Y. Zhu, L. Hu, Z. Liu, and M. Han, “Ultrasensitive ultrasound detection using an intracavity phase-shifted fiber Bragg grating in a self-injection-locked diode laser,” *Opt. Lett.*, vol. 44, no. 22, pp. 5525–5528, Nov. 2019, doi: 10.1364/OL.44.005525.

[83] H. Erzgräber, B. Krauskopf, D. Lenstra, A. P. A. Fischer, and G. Vemuri, “Frequency versus relaxation oscillations in a semiconductor laser with coherent filtered optical feedback,” *Phys. Rev. E*, vol. 73, no. 5, p. 055201, May 2006, doi: 10.1103/PhysRevE.73.055201.

[84] G. Liu, Y. Zhu, Q. Sheng, and M. Han, “Polarization-insensitive, omnidirectional fiber-optic ultrasonic sensor with quadrature demodulation,” *Opt. Lett.*, vol. 45, no. 15, pp. 4164–4167, Aug. 2020, doi: 10.1364/OL.397955.

[85] F. Karim, Y. Zhu, and M. Han, “Modified phase-generated carrier demodulation of fiber-optic interferometric ultrasound sensors,” *Opt. Express*, vol. 29, no. 16, pp. 25011–25021, Aug. 2021, doi: 10.1364/OE.432237.

[86] L. Hu and M. Han, “Reduction of Laser Frequency Noise and Intensity Noise in Phase-Shifted Fiber Bragg Grating Acoustic-Emission Sensor System,” *IEEE Sensors Journal*, vol. 17, no. 15, pp. 4820–4825, 2017, doi: 10.1109/JSEN.2017.2716410.

[87] C. Henry, “Theory of spontaneous emission noise in open resonators and its application to lasers and optical amplifiers,” *Journal of Lightwave Technology*, vol. 4, no. 3, pp. 288–297, 1986, doi: 10.1109/JLT.1986.1074715.